

**ANALYSIS OF COOLING PLATE DESIGNS
FOR FUEL CELL APPLICATIONS**

A Thesis Presented

by

Blice Nuchka Okome M'bika

Presented to the Jackson College of Graduate Studies of the
University of Central Oklahoma in Partial Fulfillment
of the Requirements for the Degree of

MASTER OF SCIENCE IN ENGINEERING PHYSICS – MECHANICAL ENGINEERING

May 2016

**ANALYSIS OF COOLING PLATE DESIGNS
FOR FUEL CELL APPLICATIONS**

A Thesis Presented

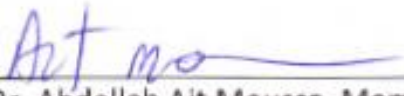
By

Blice Nuchka Okome M'bika

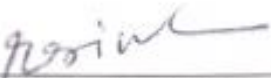
Approved as to style and content by:



Dr. Evan Lemley, Chair



Dr. Abdellah Ait Moussa, Member



Dr. Mohammad Hossan, Member

ABSTRACT

ANALYSIS OF COOLING PLATE DESIGNS FOR FUEL CELL APPLICATIONS

May 2016

Blice Nuchka Okome M'bika
University of Central Oklahoma

Directed by: Dr. Evan Lemley

ABSTRACT:

In this thesis, theoretical and computational analyses of the heat exchange in a polymer electrolyte membrane fuel cell (PEMFC) cooling plate are described. Thermal management of the fuel cells is essential to ensure high efficiency, durability, and safety of their applications. PEMFC are generally used as a power supply for vehicles in transportation, but can be extended as a back-up power system for household or corporate needs. Analysis of convective heat transfer of PEMFC cooling plates is considerably important in future optimizations techniques to develop new cooling plate designs.

Cooling plates are investigated with a method using entropy generation as a numerical analysis alternative to evaluate the performance of the cooling plate designs in addition to temperature variation, pressure drop and velocity profile. The results obtained for

the entropy generation in each designs gave effects of the frictional and thermal components of the entropy on heat transfer of cooling channels, confirmation of previous findings, and thermal and hydrodynamic fully developed regions in cooling plates. Benefits and constraints of each design are discussed followed by possible upgrades on designing cooling plates for better PEMFC performance.

ACKNOWLEDGEMENTS

This research was made possible by the Department of Engineering and Physics of the University of Central Oklahoma (UCO), under the supervision of Assistant Dean and Professor Dr. Evan Lemley. The author is grateful to Dr. Evan Lemley for monitoring and advising in the making of the report and results published in this paper. Also, special thanks to computer science student, Ivan Gutierrez for his tutoring on use of the "Buddy" cluster, and adding needed software to complete analysis in a timely fashion. The author would like to express her thanks to the undergraduate 2015/2016 Senior Engineering Design group in the Department of Engineering and Physics of UCO: *Design and implementation of an experimental apparatus to determine entropy generation for multiple fluid dynamics experiments* for setting up experimental Particle Image Velocimetry (PIV), and particularly Aric Gillispie for allowing the use of his code and knowledge in PIV for the purpose of comparing simulated to experimental result for velocity profile inside a square channel at a specified Reynolds number.

TABLE OF CONTENTS

Chapter I. SUMMARY OF LITERATURE	1
I.1 Introduction.....	1
I.2 Fuel Cell Fundamentals	4
I.3 PEMFC Manufacturing and Operations.....	8
I.4 PEMFC Heat Recovery Rates, and Effectiveness	11
I.5 Thesis Statement and Objectives	14
Chapter II. RESEARCH FOCUS	16
II.1 Thermal Management.....	16
II.2 Flow Field Designs	17
II.3 Performance Evaluation	19
Chapter III. BACKGROUND	21
III.1 Governing Equations	21
III.2 Numerical Analysis	26
III.3 Preprocessing and Flow Conditions	28
Chapter IV. STATEMENT OF THE RESEARCH METHODOLOGY	31
IV.1 Analysis	31
IV.2 Boundary Conditions	33
IV.3 Case Study	35
IV.4 PIV Validation of CFD.....	37
Chapter V. COOLING PLATE RESULTS AND ANALYSIS	43
V.1 Temperature and Velocity Outputs Comparison	43
V.2 Local \dot{S}_{gen} Analysis.....	49
V.3 Summary Tables and Figures.....	51
Chapter VI. CONCLUSION	54

LIST OF FIGURES

Figure 1: PEMFC schematic.....	6
Figure 2: Summary of thermal processes and flow paths of cooling channels	7
Figure 3: PFF model.....	18
Figure 4: SFF model.....	19
Figure 5: CPFF model	19
Figure 6: Control Volume in 2D.....	21
Figure 7: A representation of processes involved in the channel region of a cooling plate	27
Figure 8: (a) PFF, (b) SFF, and (c) CPFF cooling plate designs with extension to ensure flow is fully developed at the outlet.....	32
Figure 9: Summary of basic boundary conditions	33
Figure 10: Single channel mesh refinements.....	35
Figure 11: Grid dependency test results for single channel flow	37
Figure 12: Schematic representation of the PIV experiment	39
Figure 13: comparative result for the velocity profile obtained between PIV experiment and CFD simulation	42
Figure 14: Temperature distribution from published (a-b) vs current CPFF (c) and SFF (d) temperature distribution	43
Figure 15 Current parallel straight channels heat transfer characteristics.	44
Figure 16: Pressure distribution and Darcy friction factor along PFF channel length.....	45
Figure 17: Reynolds number and Efficiency with respect to the Overall heat transfer in	46
Figure 18: Plates performance with modified flow field designs	47
Figure 19: Temperature Inlet/outlet data along SFF extensions.....	47
Figure 20: Pressure Inlet/outlet data along SFF extensions	48
Figure 21: Volumetric entropy and temperature variations from each model.....	50
Figure 22: Performance chart based on pressure drop.....	51
Figure 23: Pressure drop of the coolant from inlet to outlet of SFF and CPFF designs when varying the Reynolds number	52
Figure 24: Temperature increase of the coolant from inlet to outlet of SFF and CPFF designs at different Reynolds number.....	52
Figure 25: Volume integral of the entropy generated in the coolant when varying the inlet velocity for SFF and CPFF designs.....	53
Figure 26: Single straight channel 4 th Mesh Residuals.....	65

Figure 27 Single straight channel 4 th Mesh graphical Contours of Static Temperature (K) of the fluid interior in ANSYS® Fluent™ .	65
Figure 28: Single straight channel 4 th Mesh Velocity Vector of Velocity Magnitude (m/s) of the top fluid surface where the symmetry boundary was applied in ANSYS® Fluent™ .	66
Figure 29: Single straight channel 4 th Mesh Plot of Velocity Magnitude vs channel width (curve length) at the top fluid surface in ANSYS® Fluent™	66
Figure 30: PFF 3 rd Mesh Velocity Vectors represented by magnitude.	68
Figure 31: PIV at L _{1(PIV)}	70
Figure 32: PIV at L _{2(PIV)}	70
Figure 33: PIV at L _{3(PIV)}	71
Figure 34: contours of the temperature distribution	73
Figure 35: Contours of the volume integral of entropy at the inlet region.	73
Figure 36: Contours of the volume integral of the temperature component of the entropy near at the inlet region.	74
Figure 37: Contours of the volume integral of the heat dissipation of entropy at the inlet region.	74
Figure 38: Contours of the temperature distribution in fluid	75
Figure 39: Contours of the volume integral of entropy at the inlet region.	75
Figure 40 Contours of the volume integral of the temperature component of the entropy near at the inlet region.	76
Figure 41 Contours of the volume integral of the heat dissipation of entropy at the inlet region.	76
Figure 42: Contours of the temperature distribution in fluid at an inlet velocity of 0.05 m/s	77
Figure 43: Contours of total entropy distribution in fluid at an inlet velocity of 0.05m/s	77

LIST OF TABLES

Table 1: Table comparison of plate materials used in PEMFC	9
Table 2: Geometries of coolant PFF used in PEMFC.....	17
Table 3: Summary of equations of Darcy factor and Nusselt number from literature	29
Table 4: Boundary conditions and bottom surface area parameters	30
Table 5 Experimental entry length and Reynolds Number for each flow rate.....	34
Table 6: Solid and fluid properties Fluid Part (Liquid water at 40°C) Solid part (Graphite)	36
Table 7: Mesh refinement standard for single channel flow.....	36
Table 8: Geometry and thermodynamics parameters	38
Table 9: Properties comparison of Sample.....	40
Table 10: Position Summary for non-dimensional analysis from channel inlet.	41
Table 11 Geometry specifications	47
Table 12: Difference in total entropy using SLT and mesh information.....	49
Table 13 Results Summary by method of Analysis.....	51
Table 14: Current data obtained for the frictional and thermal components of the total entropy generation in the coolant.....	53
Table 15: Area comparison of the interfaces created in fluent versus interface zones wall 4 and wall 4 shadow	63

NOMENCLATURE

A	Area, m^2
c_p	Specific heat capacity, $J.kg^{-1}.K^{-1}$
D_h	Hydraulic diameter, m
\vec{F}	Body force, $N.m^{-3}$
f	Friction factor
H	Channel height, m
h	Heat transfer coefficient, $W.m^{-2}.K^{-1}$
I	Current, <i>Amps</i>
k	Thermal conductivity, $W.m^{-1}.K^{-1}$
L	Length, m
M	Mass, kg
\dot{m}	Mass flow rate, $kg.s^{-1}$
Nu	Nusselt number $Nu = hD_h/k$
P	Electrical power, W
p	Pressure, Pa
\dot{Q}	Heat transfer rate, W
q''	Heat flux, $W.m^{-2}$
Re_D	Reynolds number $Re_D = \rho v D_h / \mu$
T	Temperature, K
th	Thickness, m
U	Overall heat transfer coefficient, $W.m^{-2}.K^{-1}$
V	Voltage, <i>Volts</i>
\dot{V}	Volume flow rate, $m^3.s^{-1}$

\vec{v}	Velocity vector, $m.s^{-1}$
u	x-component local velocity, s^{-1}
v	y-component local velocity, $m.s^{-1}$
w	z-component local velocity, $m.s^{-1}$
W	Channel width, m
Δ	Difference
∇	Gradient
μ	Dynamic viscosity, $Pa.s$
ν	Kinematic viscosity, $m^2.s^{-1}$
ρ	Density, $kg.m^{-3}$
ϵ	Effectiveness
Φ	Dissipation
φ	Field variable

Subscripts

<i>act</i>	actual
<i>ch</i>	channel
<i>f</i>	fluid
<i>in</i>	at the inlet
<i>m</i>	mean
<i>max</i>	maximum
<i>out</i>	at the outlet
<i>s</i>	at the surface
<i>i</i>	variable
<i>w</i>	wall

Chapter I. SUMMARY OF LITERATURE

I.1 Introduction

Scientists think that increasing average global temperatures on earth and the related climate changes are due to increased anthropogenic CO₂ emissions due mostly to energy production [1]. As a result, scientists, engineers, and others seek to find more optimal solutions to reduce undesirable waste outputs of energy production and to improve the monitoring and management of all waste outputs in general [2]. Energy companies have long been the focus of media and environmental associations when environmental degradation or disasters, such as recent earthquakes in Oklahoma, have occurred. In the past, there have been notable environmental disasters including: the oil spill in 2010 in the Gulf of Mexico, the Exxon Valdez in 1989 in Alaska, and the Three Mile Island nuclear reactor partial core meltdown in 1979 in Pennsylvania. Energy production and wastewater management cause many kinds of environmental issues around the world, for example, plant leaks or explosions, smog, and sewage leaks; each disasters that affect surrounding communities. According to the latest Intergovernmental Panel on Climate Change (IPCC) Report [1], improvements in human health will result from reducing emissions from power plants and households, improving transportation by switching to emission-free vehicles, adopting a “healthy” diet and lifestyle, and most importantly, progressive international climate policies. Otherwise, human health may be in jeopardy because of the negative environmental effects

created by energy production and water treatment, which also could lead to social unrest.

The consumer market has become aware of the consequences of energy production and energy and wastewater mismanagement. The first step in renovating the energy and water infrastructures includes improvements in energy production technologies and water treatment (pre- and post-consumer use) methods [3]. According to the IPCC 2010 Assessment Report fossil fuel combustion emissions consists of 19% Methane and 65% carbon dioxide and causes climate change, pollution, diseases, and other issues from its production, distribution and applications. Reducing those emissions could significantly help in the prevention of an average of 2.25 million deaths worldwide [1]. Researchers have found ways to use Microbial Fuel Cells (MFC) to improve the sewage system and at the same time produce electrical energy. MFC are a mean to transform chemical energy stored in microbial entities to generate power through the process of a reaction between electrons released from the microbial particles on an anode, which in turn bonds with oxygen on the cathode side to form water [4]. This innovative technology produces electrical power, water, and the waste as a fertilizer. MFCs, can also be used in processing wastewater from food manufacturing and transforming sea water into clean water, which can benefit the environment by lowering gas emissions and reducing pollutants. Another fuel cell technology for energy production are Proton Membrane Exchange Fuel Cell (PEMFC) stacks, which use hydrogen fuel to transform stored chemical energy into electrical energy, with water as

a by-product of an exothermic chemical reaction between hydrogen gas flowing into an anode and air flowing into a cathode [5].

Using PEMFCs to satisfy current energy demand requires that energy storage be maximized by improving the ion exchange between air and hydrogen, reducing the production cost, and improving thermal management in the PEMFC stacks. For PEMFC stacks to work for a long period of time, the performance and the efficiency of each cell must improve, so there is a need for this system to incorporate thermal and water management via coolant channels. One of the biggest obstacle to fuel cell technology is heating within the cell which deteriorates the cell's components. Continuous operation time of 5000 hours [5] is required for transportation applications by the United States Department of Energy (US DOE). Another obstacle to stack performance is safety issues related to hydrogen management [6]. One may investigate the thermal behavior of the coolant channels using Computational Fluid Dynamics (CFD) simulations. Each cooling plate has fluid paths, in which a coolant fluid is directed to lower the temperature of the PEMFC during heat transfer exchanges. Those path lanes are defined as coolant flow field designs. In conventional analysis, there exists a relationship between the coolant flowrate, convection heat transfer coefficient, and pressure drop across coolant flow field. In this thesis solutions are gathered using a traditional analysis, for forty five straight channels and one serpentine channel with 2 mm x 2 mm fluid square cross section channels flowing through a solid plate subject to a constant heat fluxes applied at the bottom and top plate's boundaries. The assumptions included steady state,

constant properties, incompressible Newtonian fluid, and single phase flow in a three dimensional flow field. Negligible effects included radiation and free convection. Analyses are made on a half domain with a rectangular cross sectional area and a full domain with a square cross sectional area and validated with a particle image velocimetry (PIV) experiment. Using CFD results such as the temperature and velocity distribution, different cooling plate designs may be compared in terms of Reynolds and Nusselt numbers [7]. CFD results have been compared with local experimental results and with published data. These analyses have been augmented with a Second Law of Thermodynamics (SLT) analysis of coolant channels to obtain performance data for different configurations.

1.2 Fuel Cell Fundamentals

A Proton Exchange Membrane Fuel Cells (PEMFC) stack is composed of multiple cells. Between cells are plates containing coolant channels to remove heat and improve overall stack efficiency. This thesis focuses on the heat exchange between the PEMFCs and the coolant channel plates. Figure 1 below shows how a fuel cell operates in terms of electrochemical reactions inside a PEMFC. The PEMFC generate power following the relation:

$$P = VI \tag{1}$$

Where, V is the potential of the cell which is the voltage difference among the anode and cathode electrodes, and I is the current generated by the motion of the electrons

from anode to cathode via an external circuit. The external circuit can be a wire that connects to the cell providing an electrical path. In the internal circuit the flow of electrons is regulated inside the cell by allowing ions to move between cathode and anode electrodes. Heat is generated by the electrochemical interaction, starting with a catalyst on the anode side that will activate the motion of the electrons from the hydrogen gas and get the positive hydrogen ions flowing thru an electrolyte membrane, known as the membrane electrode assembly (MEA); to then bond with the oxygen present in air after it came in contact with a catalyst on the cathode side to create water vapor. Each gas flows inside channels separated by the conductive MEA composed of a catalyst layer followed by a gas diffusion layer, on both the anode and cathode side, in contact with a membrane that prevents electrons from passing through, but allows positive hydrogen ions [8]. Bipolar plate gas channels can have multiple inlets and outlets as shown in Figure1. The hydrogen gas is supplied through the hydrogen gas channels found in the anode bipolar plate. Thus the hydrogen is flowing from the anode inlet while the oxygen gas or air is supplied from the cathode inlet which is inside the cathode bipolar plate on the other side of the MEA.

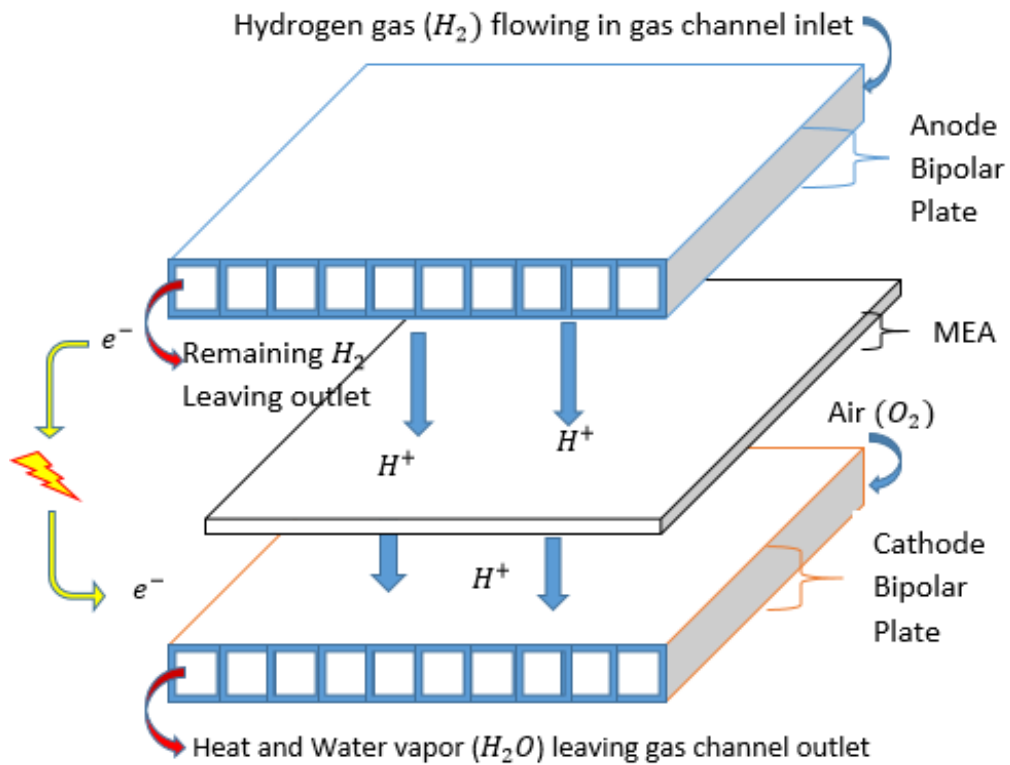


Figure 1: PEMFC schematic

Bipolar plates are current conducting plates used in PEMFC. They provide gas and coolant distribution, leakage prevention across the cell, and transports electrons from the anode of one cell to the cathode of the other cell. The strength of the current flow is dependent of the metallic conduction of the bipolar plate. Operations of PEMFC include three essential parts. First, energy is provided via cathode and anode electrodes to induce the electrochemical reaction. Second, oxidation of hydrogen gas on the anode and reduction of the oxygen ions with the hydrogen cations and electrons on the cathode occurs. Third, the electrolyte, in this case the membrane, regulates the ions motion between the cathode and anode electrodes and balance current flow in the external circuit. Cooling channels help regulate the heat produced in a Cell as shown in

Figure 2. This heat is composed of electrochemical heat generation, convection and radiation heat transfer.

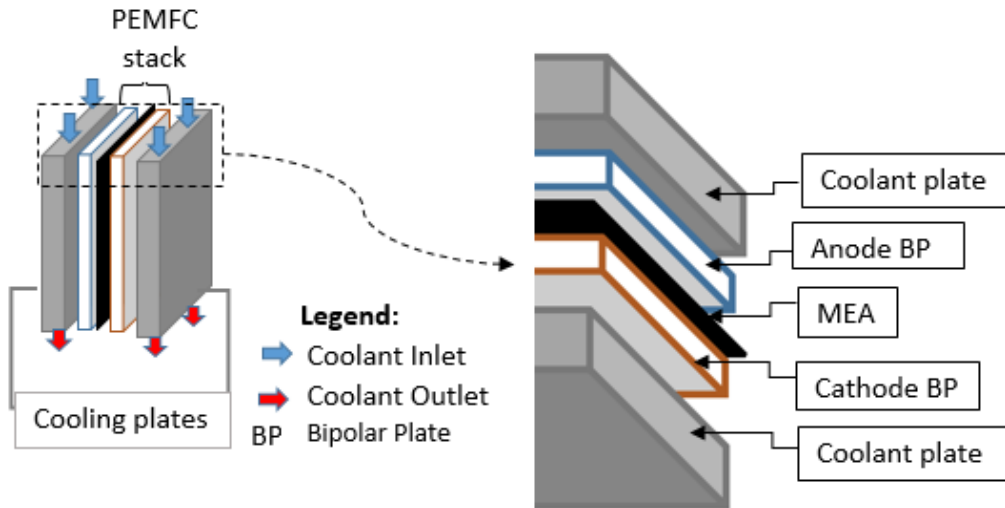


Figure 2: Summary of thermal processes and flow paths of cooling channels

To increase the performance of PEMFC the temperature distribution in cell bipolar plates must be uniform. A non-uniform temperature distribution will lead to overheating which will damage the PEMFC components and disrupt the chemical reactions that create the power output. Liquid water is often used for cooling and is driven through cooling channels, with a variety of configurations and shapes. Common shapes for cooling channels are serpentine, parallel designs, convection-enhanced serpentine flow fields (CESFF), and multi-pass serpentine flow field (MPSFF) as described by Baek [7]. Of these cooling channel designs MPSFF appears to have the most uniform temperature distribution with the same drop in pressure as the other designs. Other studies have used nanofluids as a coolant [9], a variety of different channel designs [10-12], and cooling channels with corrugations [13-18], which create chaotic flow inside the

coolant channels which ideally would increase the thermal performance of the PEMFC. Corrugations are dimples or obstructions inside a channel. The corrugations may vary from rectangular to curved shapes. Different materials have been investigated in previous researches and introduced the concept of adding corrugations for better mixing, which led to the choice of graphite overall as the material to be used for CFD simulations of the cooling plates. With corrugations better temperature distribution 60% compared to channels with flat inner faces (Channel interfaces without obstructions) and uniformity were observed and a local heat transfer increase [17].

CFD of cooling plates with different designs have been used to study flow field performance from inlet to outlet.

I.3 PEMFC Manufacturing and Operations

Design considerations for the cooling plates are closely related to their manufacturability and weight. The waste heat produced by a fuel cell occurs near the bipolar plates walls made of pure metals like aluminum, steel, composite, or graphite. The downside with metallic materials compared with composite or carbon-based materials is their thermal conductivity. Also It is a considerable issue to find ways to improve the heat transfer between cooling plates and a fuel cell because the bigger the PEMFC stack, the heavier it is, which is thus critical to manage the temperature increase in the stack while preserving the functions of a PEMFC.

Table 1: Comparison of plate materials used in PEMFC

Materials	316L Stainless steel [11]	Graphite[7]	Poco carbon [11]	Carbon graphite [19]	Aluminum [20]
$k(Wm^{-1}K^{-1})$	16.3	24	95	710	871

Bipolar plates can represent from 81% (made of coated metal) to 88% (made from graphite) of a PEMFC stacks weight compared from 1.7% to 2.6% for the membrane [12]. Also bipolar plates are the most expensive components because of the small size of channels which need to be made accurately. Manufacturing techniques include mechanical and electrochemical machining. Compression molding is an electrochemical building technique with a high production rate and cost averaging $\$200Kw^{-1}$ per plate. That is challenging because according to the US DOE a 50 Kw PEMFC stack should weight 1331kg and cost $\$35Kw^{-1}$. Furthermore, requirements in the mechanical technique, like the plate thickness should not be smaller than 3mm. Researchers have recently introduced new techniques to reduce bipolar plate thickness limitation down to 0.25mm [15]. Safe operations of liquid cooled PEMFCs occur between 60°C and 80°C of a stack's temperature. Also, higher temperatures the PEMFC components will begin to deteriorate. Higher performance of a stack containing 4 cells between cooling plates was observed between 5°C and 20°C of temperature variance with countercurrent flow versus concurrent flow [21]. O'Keefe et Al. reported a 96.5% reduction in stack's temperature difference when introducing a controller to adjust inlet coolant flow rate to maintain the stack temperature at 350K, a value close the maximum 80°C operating

condition [22]. The controller worked well, and allowed the temperature to vary by less than 3K from optimal stack temperature condition. This system is not as efficient if the coolant fluid, in this case water, is reused into the PEMFC, and with low current generation. Overall it still works better than not having a controller. Thermal limitation on PEMFC is due to the sustainability of the PEM which currently ranges from 50°C to 100°C and other scientists have claimed to reach 120°C from their research [23]. Controlling the pressure drop inside the cooling plate prevents flooding or drying the MEAs of a stack. Water cooling for fuel cell applications has been more effective than air cooling. Recycling of the water used to cool PEMFC using a condenser and increasing the flow rates have a 44% greater efficiency compared to keeping constant flow rates during removal of excess heat [24].

This thesis experimental Particle Image Velocimetry (PIV) data were obtained to study the liquid flow in a single channel without heat transfer consideration. Also, PIV allowed testing boundary conditions near the wall of a cooling plate and assumptions made in CFD. However, if a PEMFC experiment was carried out, the pieces of equipment used to operate a PEMFC for automotive application would include coolant pumps to push the liquid in and out the PEMFC, radiators or fans, hydrogen blower to supply PEMFC at the hydrogen inlet, gas cooler to cool the outlet heated gases and circulate them back into the PEMFC [21]. Health and safety standards have to include proofing the gas channels so that the excess hydrogen gas is successfully collected at the outlet and sent back to the inlet to undergo the chemical exchange reactions. The heat

produced by the reactions may not be a hazard for the surroundings but has to be properly extracted out of the PEMFC in a form of hot water vapor as Figure 1 suggest in a manner of which it can be reintroduced in the PEMFC in a new form (Cooled liquid water) in order to create a production environment free of waste, for instance.

The cyclic method of operation proposed above is yet another critical component that affects the weight of the overall PEMFC and may rise structural reliability concerns. In the end, it is not a question of whether or not use PEMFCs, it is a matter of what to address in order to popularize the use of PEMFCs. Implications and regulations include a small weight, an easiness of construction, and simple design. Those of which have been investigated in this thesis.

I.4 PEMFC Heat Recovery Rates, and Effectiveness

For refinery uses it is important to recover most of the energy applied into a heat exchanger. For oil and gas processing, improvements have been made to reduce carbon dioxide emissions. For example, to improve the energy balance for shell and tube heat exchangers, tube designs include multiple passes in condenser section. Adjusting the turbulence and wall shear stress can help reduce fouling inside the tubes, thus improving the overall heat transfer in the heat exchanger. Similarly, plate heat exchangers (PHE) have been used to cool heated microscale chips, using different flow patterns, plate materials, or adding corrugations inside the flow channels of the PHE to increase heat transfer. However, in PEMFC, in addition to heat transfer processes

encountered in the previously mentioned applications, the solid material in the cooling plates is subject to electrochemical forces that can deteriorate the plate itself. The heat generated and the electrochemical forces have to be taken into account. For that reason the volume of the plate is increased by adding more cells between the cooling plates, thus the cost of a PEMFC increases as well. Some advances in PEMFC's could help extend fuel cell technology to large scale applications leading to the construction of fuel cell power plants. Such aim requires material, flow path and thermal analysis that can be tested using automotive efficient PEMFC radiators by reducing their weight and increasing the uniformity of the temperature distribution in both cooling and heating processes. Studies on air cooling performance [20, 23, 25, and 26], on the channel flow field demonstrated that the 3-D mixing and bend angle at each location where the flow changes direction within cooling channels and the number of those changes will have an effect on coolant streamlines which depends on the fluid flow velocity. Such effects, for example, the average temperature and the uniformity of the temperature distribution of the air cooled plate decreases as the Reynolds number increases [20]. Similar results are expected for liquid cooled plates. Several cooling channels have been studied in previous work related to increasing the effectiveness of the heat exchange between the cooling agent and fuel cells [21].

For the case of heat sinks used in laptops, the more transistors a microchip has the faster it operates and gets heated. The chip will during operation warm the heat sink and the heat sink will warm the air flowing through so that the warm air will dissipate

out of the chip. However, because of the noise that fans tend to make and the power required for cooling heated components a research emphasis has been made on liquid cooling rather than gas cooling in this paper. The efficiency of PHE can be improved using nanofluids as a result of a better convection and mixing fluid [9].

Entropy generation within the cell has been investigated [27-28] and the entropy generation fluctuations within a PEMFC stack decrease or increase the performance of a PEMFC. Changes in entropy occur after heat is generated and during the cooling of the PEMFC. The humidity between the MEA and the bipolar plates keeps the membrane from dehydrating, which means heat has to be removed. At the same time the membrane water content can lower the power output in the process if an excessive amount of heat was removed from the cell because it will cause flooding near the MEA and prevent chemical reactions from occurring. A PEMFC operating at 0.7 V can generate $20,000 \text{ Wm}^{-2}$ of heat flux and that heat flux is the heat generated by the PEMFC [24]. Other studies looked at entropy distributions when varying the humidity at the membrane to investigate how the entropy generation due to both heat and mass transfer could affect the operations of a PEMFC [27]. Mostly, heat dissipation that contains frictional components in the entropy equation from heat transfer is found to be more influential than the entropy due to mass transfer. The dissipation increases with the viscosity of the fluid and also the mixing within PEMFC channels and the lower the entropy generation rates the higher the thermal performance of a system will be. The study also has shown that entropy due to mass transfer depends on the

concentration of the gases involved in the chemical process. High concentrations increase the current density, which leads to high temperature gradients, which leads to high entropy generation. Also, when the current produced increases as the humidity increases, but the current stops increasing as the total entropy rises because of the surge in heat transfer rates, which reduces efficiency of the functions of the PEMFC. Consequently, entropy generation management is critical in the study of cooling plates for fuel cell applications.

I.5 Thesis Statement and Objectives

In this project a Second Law of Thermodynamics (SLT) analysis technique was used to get the maximum performance of a heat exchanger for a given size and power input for the cooling plates. Local characteristics of heat transfer from CFD and entropy generation from SLT analysis were evaluated to improve heat exchanger performance.

The Thesis objectives are:

1. Successfully simulate multiple model designs of a PEMFC cooling plate heat exchanger by setting up boundary conditions, recording output, and analyzing the results.
2. Modify the Reynolds number to observe changes of the fluid behavior inside the cooling plate channels.
3. Perform PIV experiment to validate the CFD simulations for velocity magnitude inside channels

4. Determine local temperatures and velocity profiles, overall heat transfer, and entropy generation rates.
5. Analyze heat transfer variation from modified designs.

Chapter II. RESEARCH FOCUS

II.1 Thermal Management

The heat generation rate in a cell is the difference between the cell voltage output, assuming the electrochemical reactions are totally transformed into electrical energy, also known as thermal voltage and the cell operating voltage; increased by the current density[21]. Computational analysis using ANSYS® Fluent™ is used to get the different parameters to understand thermal effects of PEMFC stacks. However, the thermal properties of the liquid, gaseous, and solid elements of a cell can vary a lot during operations compared to simulations because of factors such as materials availability from different suppliers, compression of cell's components in a PEMFC stack, and water content, and distribution that can affect with the PEMFC performance. The water content in bipolar plates matters.

For water-cooled PEMFC plates [6, 22, 29-30] simulations under laminar conditions have shown that if heat flux on cell surface increases, initial fluid properties used to get the inlet velocity will differ from the inlet cold fluid. Several liquid-cooled bipolar plates have shown to be 40 to 50% effective to decrease heating effects on a PEMFC stack. The cooling channels studied in previous experiments related to fuel cells to increase the effectiveness of the heat exchange happening between the cooling agent and fuel cells were in most part showing similar velocity and temperature profile for each respective channel design. Their results will be needed to validate the simulations in the paper.

II.2 Flow Field Designs

This thesis will study water cooling channels with serpentine flow field (SFF) and parallel flow fields (PFF) with small modifications to better analyze the two different flow fields. Scientists have concluded serpentine channels have a better temperature distribution [10, 20-21]. At higher values of both heat flux and flow rates, serpentine configurations perform better in terms of temperature uniformity. In addition, SFFs improve heat transfer compared to PFF and other designs. Variations of the serpentine model which has a single channel inlet for its design included multipass serpentine (serpentine flow path with more than one channel inlet), divided serpentine (serpentine flow path covering the plate in quadrant sections separately) and distributed serpentine (serpentine flow path covering the plate in two separate section) to cite only a few. Serpentine flow channels prevent liquid water formation via condensation [12] in the cathode channels of PEMFC because water vapor formed in the region does not have room to accumulate when flowing through a bipolar plate with a single channel SFF. The SFF forces the water byproduct to pass thru the cathode bipolar plate which reduces changes of having regions water buildups in the channel.

Table 2: Geometries of coolant PFF used in PEMFC

Reference	Number of Channels	Channel Length (mm)	Cross section (mm^2)
[30]	50	100	1x1
[7]	45	180	2x2
[25]	29	180	3x1

The first design considered in this thesis was a PFF (Refer to Table 2 in [7]) consisting of a number of straight parallel channels. Though it is simple to build, it can be challenging to simulate. PFF channels are the easiest to make and produce low pressure drops from inlet to outlet. Following a recent study approach and making sure the laminar condition was respected the inlet velocities tested for SFFs and Combined Parallel Flow fields (CPFFs). The surface area where the heat constant heat flux is applied on the bottom plate is the same as well as the solid surface in contact with the fluid in both designs. Figure 3 was designed following the geometry specified in [7] and was used to validate CFD simulation. Figures 4 and 5 were designed using the same plate surface area used for PFF design in figure 3.

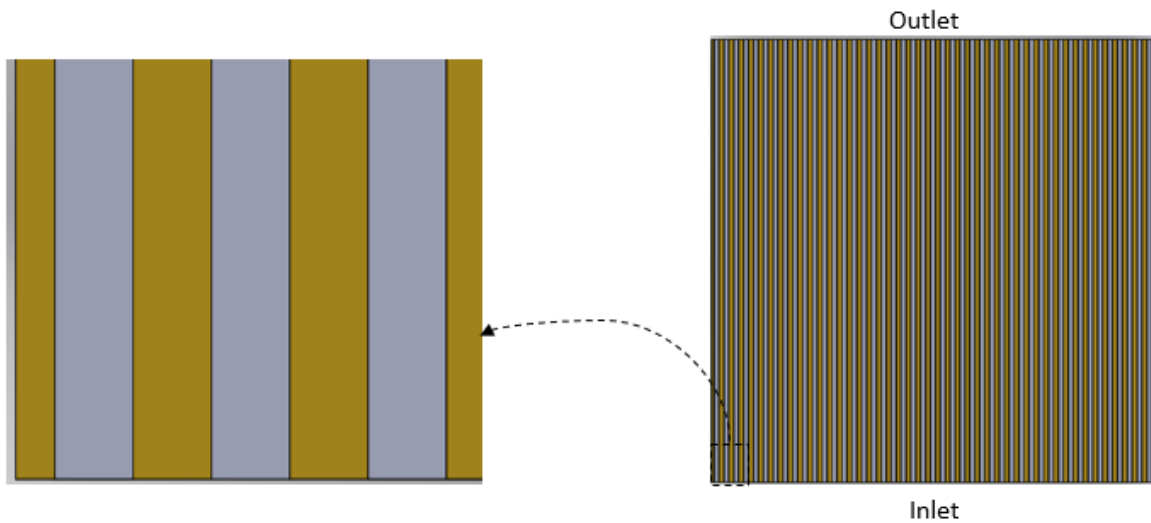


Figure 3: PFF model

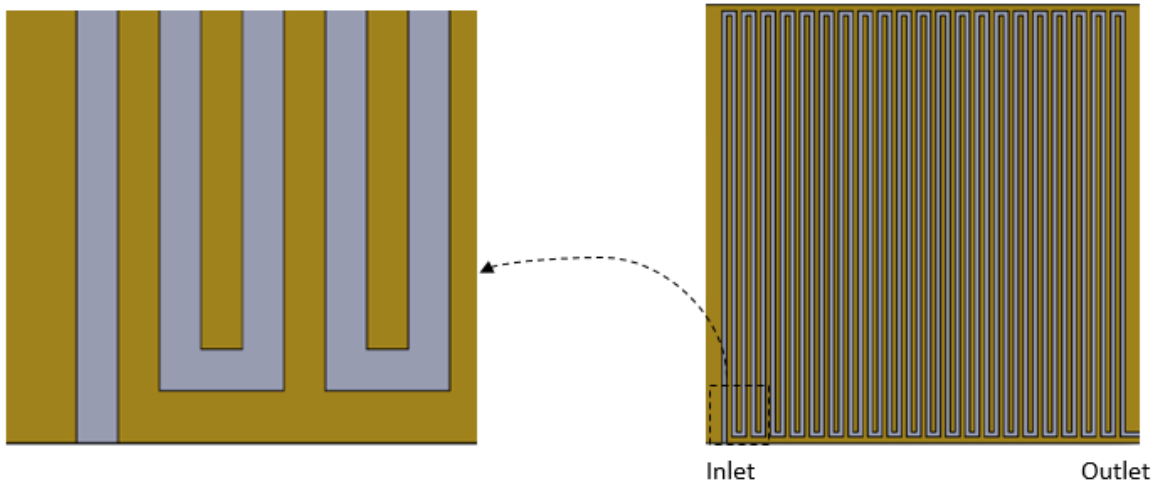


Figure 4: SFF model

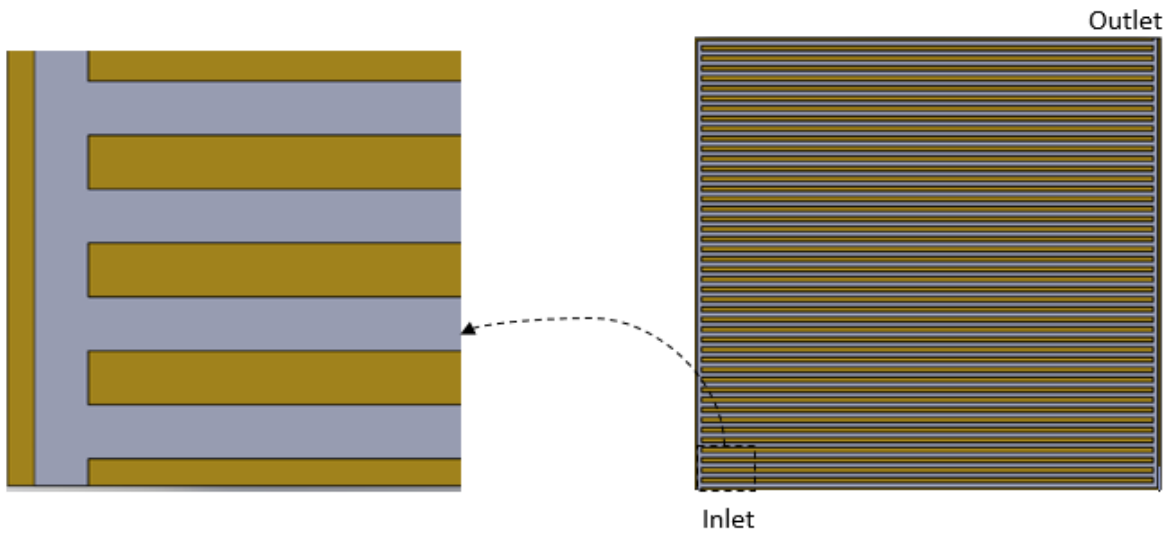


Figure 5: CPFF model

II.3 Performance Evaluation

CFD with ANSYS® Fluent™ gives the different parameters to understand thermal effects of water-cooled PEMFC plates. Previous researches with laminar flow have shown that if heat flux on cell surface increases, initial fluid properties used to get the

inlet velocity will differ from the inlet cold fluid. Although those properties are still assumed to be constant in theory, this thesis has studied water cooling channels with changes in the flow field. In addition to that, heat transfer effects when varying the cooling plate geometry such as connecting channels in the PFF and making a combine PFF (CPFF) design by increasing channel's length.

Advances in PEMFC is the plate heat exchanger problem that could help extend fuel cells technology to large scale applications leading to construction of fuel cells power plants. Such aim requires material, flow path and thermal analysis that can be tested using automotive PEMFC by reducing the weight and increasing the uniformity of the temperature distribution in both the cooling and heating processes. A study on the channels flow field demonstrated that three-dimensional (3D) mixing and bend angle at each turn within channels, as well as the number of turns affects the streamlines motion which depends on the fluid flow velocity. It is found that the average temperature and the uniformity of the temperature distribution of the Air cooled plate where the heat is applied decreases as the Reynolds number increases [20]. Similar results are expected for liquid cooled plates [14]. Some PEMFC have cooling bipolar plates added to decrease heating effects on a PEMFC stack. Several cooling channels have been studied in previous experiments related to fuel cells to increase the effectiveness of the heat exchange happening between the cooling agent and fuel cells.

Chapter III. BACKGROUND

III.1 Governing Equations

The Figure 6 below show how the fundamental principle to solve the energy equation applies to the control volume (cv).

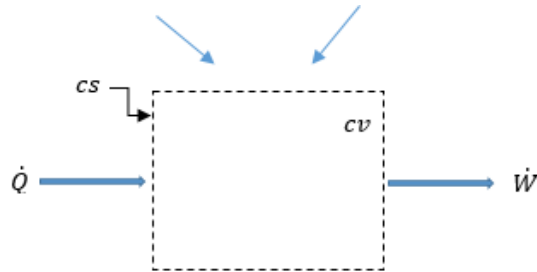


Figure 6: Control Volume in 2D

- **Continuity equation**

The mass flowrate through area, A on a control surface, cs is given by:

$$\dot{m} = \int \rho \vec{v} \cdot d\vec{A} \quad (2)$$

The conservation of mass from thermodynamics given as:

$$\frac{\partial M_{cv}}{\partial t} = \sum \dot{m}_{in} - \sum \dot{m}_{out} \quad (3)$$

Using a small control volume to get the velocity and temperature distribution near the walls, for three dimensional (3D) flow field, the control volume is therefore a parallelepiped made of $\Delta x \Delta y \Delta z$. Using local components of the velocity in rectangular coordinates gives the local mass conservation principle when the density is constant.

$$\rho \nabla \cdot \vec{v} = \rho \left(\frac{\partial u}{\partial x} + \frac{\partial v}{\partial y} + \frac{\partial w}{\partial z} \right) = 0 \quad (4)$$

Thus, the material derivative of density derived from the conservation of mass is as:

$$\frac{D\rho}{Dt} = \frac{\partial\rho}{\partial t} + \frac{u\partial\rho}{\partial x} + \frac{v\partial\rho}{\partial y} + \frac{w\partial\rho}{\partial z} = 0 \quad (5)$$

- **Momentum equation**

The momentum equations are equations used to determine fluid velocity throughout the control volume. To compute the entire assembly made of fluid and solid domain one needs to rely on the material properties as well as the changes in the velocity field. Conservation of momentum applied to the cv gives:

$$\frac{\partial}{\partial t}(M\vec{v}_n)_{cv} = \sum \vec{F}_n + \sum_{inlet}(\dot{m} \vec{v}_n) - \sum_{outlet}(\dot{m} \vec{v}_n) \quad (6)$$

With n the direction of analysis (\vec{v}_n, \vec{F}_n). The momentum equation in one direction (x) is:

$$\frac{D(\rho u)}{Dt} = \frac{\partial(\rho u)}{\partial t} + div(\rho u \vec{v}) = div(\mu \nabla u) - \frac{\partial p}{\partial x} + \vec{F}_x \quad (7)$$

With the assumptions that the fluid is incompressible and that the absolute viscosity μ is a constant equation 7 becomes:

$$\frac{\partial(\rho uu)}{\partial x} + \frac{\partial(\rho vu)}{\partial y} + \frac{\partial(\rho wu)}{\partial z} = \mu \left[\frac{\partial^2 u}{\partial x^2} + \frac{\partial^2 u}{\partial y^2} + \frac{\partial^2 u}{\partial z^2} \right] - \frac{\partial p}{\partial x} + \vec{F}_x \quad (8)$$

- **Energy equation**

The energy of a particle is derived by computing its internal energy (kinetic or potential energy for example) and external energy (heat or work added to the system). The first law of thermodynamics state that energy can only be transformed from one form to another and it cannot be created or destroyed. Under the same assumptions as in equation 8 and conservation of mass equation, the most general form of the energy

equation is the material derivative of energy times the density of the particle which produce the following:

$$\rho \frac{De}{Dt} = \mu\Phi - \text{div}(k\nabla T) + q''' + \mu\Phi \quad (9)$$

The dissipation Φ is caused by shear stress in the fluid and is computed using the gradient in local velocities in all directions of the fluid flow. Those velocity gradients are responsible for fluid energy dissipation which varies depending on the viscosity of the fluid. In 3D one obtains the following:

$$\begin{aligned} \Phi = 2 \left[\left(\frac{\partial u}{\partial x} \right)^2 + \left(\frac{\partial v}{\partial y} \right)^2 + \left(\frac{\partial w}{\partial z} \right)^2 \right] &+ \left[\left(\frac{\partial u}{\partial y} + \frac{\partial v}{\partial x} \right)^2 + \left(\frac{\partial v}{\partial z} + \frac{\partial w}{\partial y} \right)^2 + \left(\frac{\partial w}{\partial x} + \frac{\partial u}{\partial z} \right)^2 \right] \\ &- \frac{2}{3} \left(\frac{\partial u}{\partial x} + \frac{\partial v}{\partial y} + \frac{\partial w}{\partial z} \right)^2 \end{aligned} \quad (10)$$

The third component in equation 10 contains the mass conservation thus it disappears from the dissipation equation. The viscous stress components in the energy equation are derived from linear and volumetric changes of a particle said to have a Newtonian and compressible flow. Properties such as dynamic viscosity μ and “second” viscosity λ emerge in order to relate the viscous stress components to those changes as follows:

$$\tau_{xx} = 2\mu \frac{\partial u}{\partial x} + \lambda \text{div} \vec{v} \quad (11)$$

$$\tau_{xy} = \tau_{yx} = \mu \left(\frac{\partial u}{\partial y} - \frac{\partial v}{\partial x} \right) \quad (12)$$

Using the empirical relations τ_{xy} and σ_x and by rearranging the results from the viscous stress components, adding the effects from the second viscosity which are relatively

small to the body force term. The energy equation leads to Navier-Stokes simplified equation when fluid is assumed to be Newtonian and incompressible, 1D gives:

$$\rho \frac{Du}{Dt} = -\frac{\partial p}{\partial x} + \text{div}(\mu \nabla u) + \vec{F}_x \quad (13)$$

With μ is constant and $\vec{F}(x, y, z)$ and $\vec{v}(x, y, z)$, the 3D formulation is as:

$$\rho \frac{D\vec{v}}{Dt} = -\nabla P + \mu \nabla^2 \vec{v} + \vec{F} \quad (14)$$

Using these results in the first law of thermodynamics, the energy accumulated in the three dimensional control volume is reduced to:

$$E = \rho c_p \frac{DT}{Dt} \quad (15)$$

Using the 1st Law of thermodynamics the energy equation becomes:

$$\rho c_p \frac{DT}{Dt} = -\nabla \cdot q'' + q''' - P \nabla \cdot \vec{v} + \mu \Phi \quad (16)$$

Knowing that the internal heat generation q''' is negligible in this case, the heat flux

$q'' = k \nabla T$, and from mass conservation $\nabla \cdot \vec{v} = 0$. The energy equation finally reduces to:

$$\rho c_p \frac{DT}{Dt} = -k \nabla^2 T + \mu \Phi \quad (17)$$

- **Entropy Accountings**

The concept of entropy was developed by Rudolf Clausius, a German physicist and mathematician, in 1865 when he introduced the Second Law of Thermodynamics (SLT).

The First Law of Thermodynamics (FLT) include the continuity and energy equations which in many cases are sufficient for convective heat transfer problem solving in the fluid region. Otherwise, knowing that energy is neither created nor destroyed, that is to say what goes in the system must come out it; another effect known as irreversibility:

entropy could be useful in finding the temperature and velocities fields. In this thesis, we will use those fields obtained in CFD to measure the entropy in an aim to investigate how to reduce the pumping power while improving thermal contact in the heat exchanger (cooling plates). Entropy is affected by the kinetics of a particle or its motion. The more the particle is moving the more its entropy increases. By increasing its temperature the solid changes to liquid phase and eventually into a gas, each successive phase with greater entropy. The general form of SLT for a control volume is:

$$\frac{\partial S_{cv}}{\partial t} = \sum \frac{Q_{in}}{T_{in}} + \sum_{in} \dot{m}s - \sum_{out} \dot{m}s + \dot{S}_{gen} \quad (18)$$

This form does not include irreversibility associated with lost work because this study of the cooling plates does not involve external work. Following the same procedure from the energy equation that ended in equation 17, the same can be done to derive the form of \dot{S}_{gen} by considering mechanical irreversibility: heat transfer and friction.

$$\dot{S}'''_{gen} = \dot{S}'''_{gen}(Thermal) + \dot{S}'''_{gen}(Frictional) \geq 0 \quad (19)$$

$$\dot{S}'''_{gen} = \frac{k}{T^2} (\nabla T)^2 + \frac{\mu}{T} \Phi \geq 0 \quad (20)$$

With Φ defined in equation 10 and $(\nabla T)^2$ in 3D given as

$$(\nabla T)^2 = \left[\left(\frac{\partial T}{\partial x} \right)^2 + \left(\frac{\partial T}{\partial y} \right)^2 + \left(\frac{\partial T}{\partial z} \right)^2 \right] \quad (21)$$

III.2 Numerical Analysis

The algorithm used in CFD to solve for the temperature, velocities and pressure field of the designs proposed above was SIMPLE algorithm that is a pressure and velocity scheme enabled in the solution method. This scheme is used for single phase flows. The implementation of the algorithm relies on its resolution. The model domain was half of the actual size of the cooling plate as shown schematically in Figure 7. This model acknowledges for simplified CFD algorithm, where some components of the momentum equation are guessed (Pressure) at the beginning of the calculation, then replaced by a corrected value through the interpolation process. The same technique is used for the continuity equation solved in fluent. In some cases where the SIMPLE algorithm solution does not converge (Divergence detected), one way to go around it is to modify the relaxation factors for momentum and pressure used in the iterations.

There are two types of cooling processes occurring in a PEMFC stack. The active cooling due to the performance of cooling channels and the passive cooling due to the heat dissipated by natural convection and radiation of the heat flux created from the electrochemical reactions as shown in Figure 7.

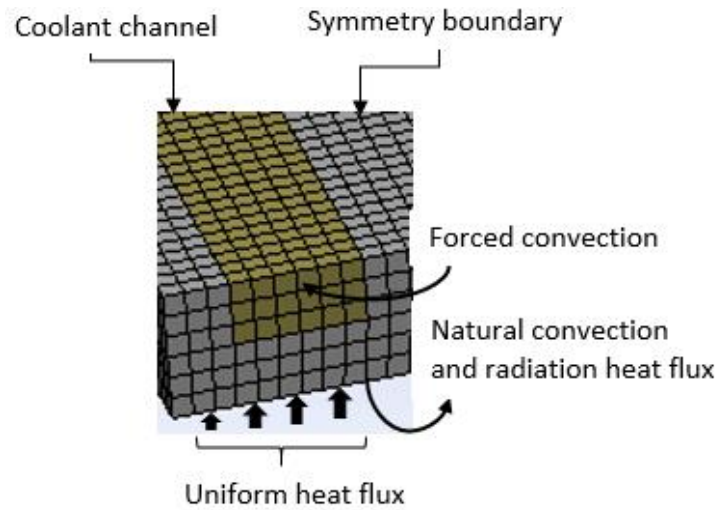


Figure 7: A representation of processes involved in the channel region of a cooling plate. Natural convection and radiation heat flux released are neglected in the simulation to look at the effects of just the cooling, in order to compute the most heat the cooling plate can remove when subject to a uniform heat flux coming from PEMFCs. Free convection and forced convection occurs inside the cooling plates' channels and heat conduction occurs when the energy produced by the PEMFC is collected by the current flowing through the walls of a cell bipolar plates and MEA [19].

The heat transfer that varies based on the profile of the water distribution is strongly relying on the coupling between the fluid and solid interface. The temperature gradient and average temperature across the cooling plate can change the thermodynamics properties of the components of a PEMFC (materials and condition of operations) [21]. Furthermore, it controls the heat transfer and temperature profile across the cooling plate, and therefore the efficiency of the Cells.

III.3 Preprocessing and Flow Conditions

The assumptions made were steady state in which there is no time component, Newtonian fluid and incompressible flow which serves in the mass conservation, heat transfer condition in which all the heat added into the control volume in this case the fluid part has to come from the solid part.

Using the momentum Equation 8, the energy equation 17, the continuity equation 5, parameters such as Nusselt number and friction factors can be derived temperature and pressure results in Fluent.

From Newton's law of cooling

$$q'' = h(T_s - T_m) \quad (22)$$

For fully developed flow conditions and q'' constant

$$\frac{dT_s}{dx} = \frac{dT_m}{dx} \quad (23)$$

After the simulation is completed the mean temperature can be derived by using:

Two point forward difference

$$\frac{dT_m}{dx} = \frac{T_{m(i+1)} - T_{m(i)}}{dx} \quad (24)$$

Two point central difference

$$\frac{dT_m}{dx} = \frac{T_{m(i+1)} - T_{m(i-1)}}{dx} \quad (25)$$

The pressure drop results were also calculated from the two point central and forward difference and compared to the ones computed by numerical method and both matched. Next step consist of computing the Nu and f with the Nusselt number and the

Darcy factor equations used for the analysis can be found in [7] and are necessary to evaluate the thermal and hydrodynamic performances of the designs across the channel. Notice that the mean temperature gradient are used and taken from equations 24 and 25. The two point central has a higher precision in finding those temperature gradients.

$$Nu = \frac{dT_m}{dx} \frac{\rho c_p \bar{v} / A_{ch} D_h}{k P_{ch} (T_s - T_m)} \quad (26)$$

$$f = \frac{dp}{dx} \frac{D_h}{\rho \bar{v}^2 / 2} \quad (27)$$

Table 3 shows methods applied in literature to get the Nusselt number and friction factor found in this thesis using equations 26 and 27. Table 4 show the main boundary conditions applied on the different geometries investigated in this thesis.

Table 3: Summary of equations of Darcy factor and Nusselt number from literature

Ray et al. [9] Darcy friction factor and Nusselt number correlations for PHE on a single phase fluid.	$Nu = \begin{cases} 1.67 Re^{0.44} Pr^{1/2} & 45 < Re < 300 \\ 0.405 Re^{0.7} Pr^{1/2} & 300 < Re < 2000 \end{cases}$ $f = 0.30025 + \frac{91.75}{Re} \quad 50 < Re < 1800$
Poulikakos et al. [31] The exact Darcy friction factor and Nusselt number for a squareduct for steady state, laminar, incompressible and fully developed flow conditions with the viscosity maintained constant.	$f \cong 56.908$ $Nu = 3.095$
Hooman et al. [32]	$Nu = \frac{q'' D_h}{k(T_w - T_m)}$

Table 4: Boundary conditions and bottom surface area parameters

Inlet velocity sample (ms^{-1}) for $Re_D = 30$	0.06
Inlet velocity cooling plate (ms^{-1}) for $Re_D = 135$	0.05
Wall heat flux sample ($Wm^{-2}K^{-1}$) for $Re_D = 30$	5000
Wall heat flux cooling plate for $Re_D = 135$	5000
Surface area for sample (m^2)	0.00036
Surface area for SFF, CPFF and PFF (m^2)	0.0324

Chapter IV. STATEMENT OF THE RESEARCH METHODOLOGY

IV.1 Analysis

A case study with a $2 \times 180 \text{ mm}^2$ channel was completed to examine the conditions to be given to the simulated cooling plates and correlates CFD simulations with PIV. For CFD simulations it is important to decide on the inlet velocity for each design. In order to make them equivalent to each other the inlet velocities depends on the channel size and number of inlets. For example, PFF has 45 straight channels thus each channel cover a side of the cooling plate. To compare results with those from literature their inlet velocity had around 0.05 m/s. SFF design has only one channel and in order to correlates with the PFF results the inlet velocity had to be close to 3 m/s. SFF and CPFF both have one inlet and one outlet thus the same inlet velocity approach was used to simulate both models. This thesis also looks at entropy, thus in the analysis the extreme case for CPFF and SFF designs was computed in CFD for 0.05 m/s, the same used in PFF to compare entropy generation is all three designs under same exact boundary conditions. This computation is referred in this thesis as “extreme” because the temperature difference between inlet and outlet is over 500K for both CPFF and SFF at an inlet velocity of 0.05 m/s. By increasing the flowrate the difference in temperature is reduce. Thus the inlet velocity flowrates were varied for SFF and CPFF models from 0.05 m/s to 0.1 m/s, 0.2 m/s, and 0.3 m/s. Those produced results for safe operations of PEMFC.

- **Modified Models**

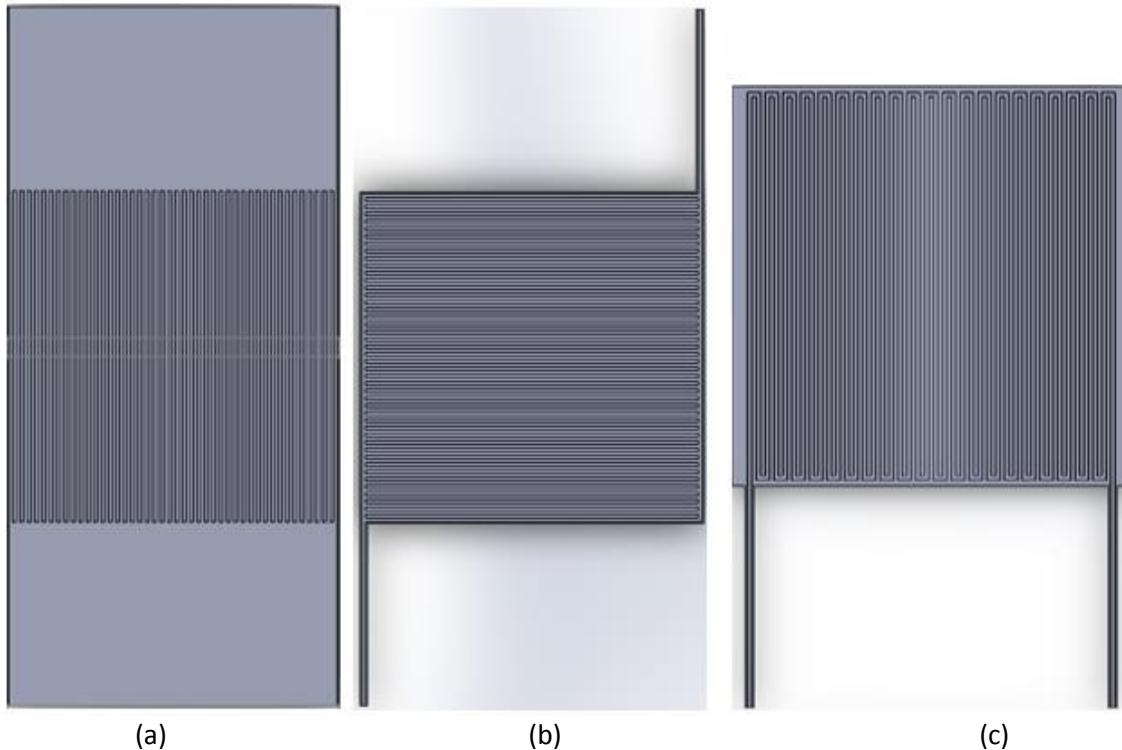


Figure 8: (a) PFF, (b) SFF, and (c) CPFF cooling plate designs with extension to ensure flow is fully developed at the outlet

For Each simulation ANSYS® Fluent™, reference values such as inlet temperature, and velocity of the fluid part are assigned. More information about other boundaries conditions are listed on Table 4. Extensions were added to ensure that the fluid was fully developed at the outlet that was subject to an outflow condition. Refer to Figure 8.

After the calculation converges, noting that the convergence will vary with the mesh size, the mass weighted average of the static temperature of the fluid and the area weighted average of the solid at different locations in the channels are computed, by using the surface integrals option. Fluent will derive it with Mass Weighted average and Area weighted average shown respectively in equations 28 and 29.

$$\frac{\int \varphi \rho |\mathbf{v} \cdot d\vec{A}|}{\int \rho |\mathbf{v} \cdot d\vec{A}|} = \frac{\sum_{i=0}^n \varphi_i \rho_i |\vec{v}_i \cdot \vec{A}_i|}{\sum_{i=0}^n \rho_i |\vec{v}_i \cdot \vec{A}_i|} \quad (28)$$

$$\frac{1}{A} \int \varphi dA = \sum_{i=0}^n \varphi_i |A_i| \quad (29)$$

IV.2 Boundary Conditions

After designing cooling plates and flow field in SOLIDWORKS® the fluid and the solid bodies created are assembled and their interfaces and surface boundaries identified. After the meshing, the properties of the fluid are set up for water and the solid part defined by the wall surface is defined as Graphite. Half of the domain of the surfaces and volumes boundaries are simulated in ANSYS® Fluent™ making use of symmetry of the results in the y-direction of the geometry subject to heat transfer as interpreted by Baek [7].

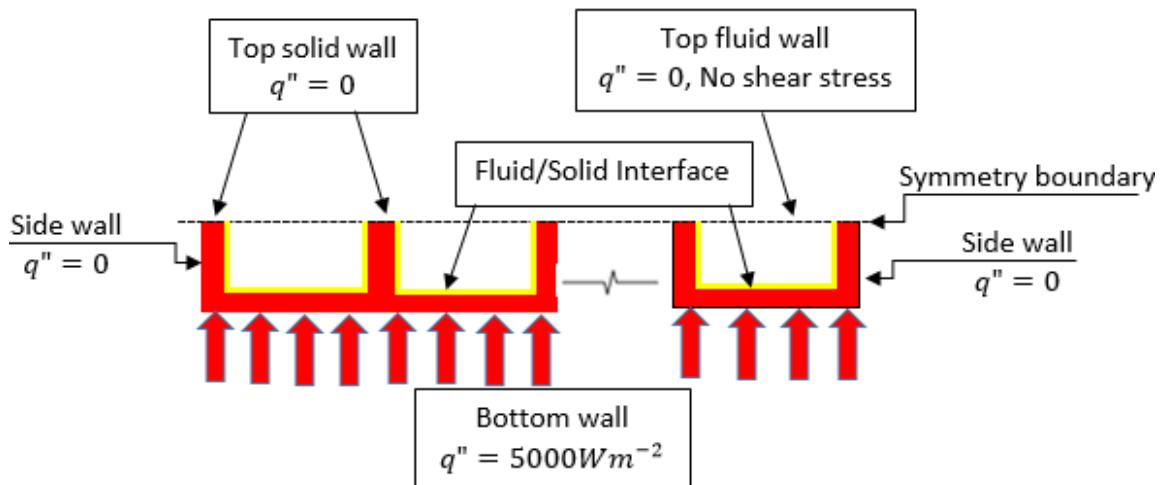


Figure 9: Summary of basic boundary conditions

After defining a fluid interface and a solid interface for the meshing as shown in Figure 9, a contact region must be set up in fluent, combining both solid and fluid separate

interfaces into one contact region. More information about interface set up is explained in Appendix B. The outflow condition assigned to the outlet, can be checked for each value of inlet velocity used in the experiment, by computing \dot{m}_{out} and \dot{m}_{in} . If they are equal the outflow condition is verified.

The simulation is carried out assuming laminar condition. To verify this assumption the flow rate the entry lengths were computed for different inlet velocity for the design in Figure 3 results are shown in Table 5.

Table 5: Experimental entry length and Reynolds Number for each flow rate

heat flux	Vdot	mdot	V(m/s)	Re	(Le)min
5000	3.00E-06	3.00E-03	0.12	598.2054	0.149551
5000	2.00E-06	2.00E-03	0.08	398.8036	0.099701
5000	1.00E-06	1.00E-03	0.04	199.4018	0.04985
5000	7.50E-07	7.50E-04	0.03	149.5513	0.037388
5000	5.00E-07	5.00E-04	0.02	99.7009	0.024925
5000	2.50E-07	2.50E-04	0.01	49.85045	0.012463

Another part of this study involves studying modified designs shown in Figure 8 to account for the case where inlet and outlet are extended to ensure the flow is fully developed before entering the PEMFC cooling plates region to study effects on PEMFC cooling. The cooling plate material selected was graphite. A comparison of the temperature distribution over the cooling plates by changing the heat flux applied to the cooling plate. As shown in the analysis provided in the Appendix. Increasing the heat flux over the fluid body reduces the inlet temperature if the Reynolds number is to be kept constant. It is a good process since the power required to produce the required

mass flow rate is also going to decrease. The results shown in Appendix C are biased in terms of getting the Nusselt number to converge.

IV.3 Case Study

The first step in simulating the coolant channel heat transfer and investigating the results consisted of making a simple geometry. The chosen geometry, denoted in this thesis as Sample, comprised of a solid and fluid part. Table 6 has the properties.

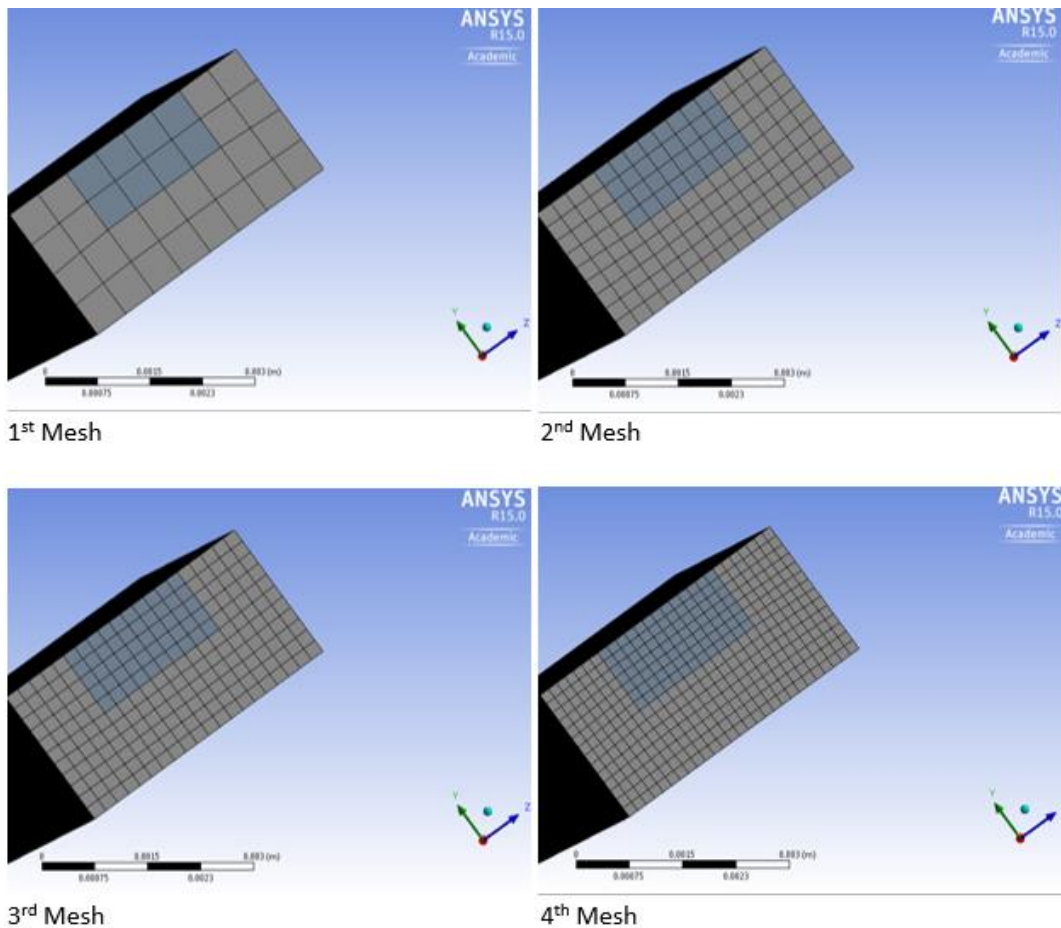


Figure 10: Single channel mesh refinements

Table 6: Solid and fluid properties Fluid Part (Liquid water at 40°C) Solid part (Graphite)

Properties	Solid part (Graphite)	Fluid Part (Liquid water at 40°C)
ρ (kg/m^3)	2250	992.2
c_p (J/kgK)	690	4179
k (W/mK)	24.0	0.62

The second step was to refine the mesh of the Sample model in order to get results that will not vary by making a finer mesh that the final mesh picked to report findings in parameters such as velocity and temperature, for example. In this case study the final mesh obtained was mesh 4 shown in Figure 10. The stopping factor was deduced based on a percent error calculation carried for both the maximum velocity and outlet pressure data of Sample with equation 30. Graphical results are displayed in Table 7 and Figure 11.

$$\% Error P_{outlet} = \left| \frac{P_{outlet(n)} - P_{outlet(n-1)}}{P_{outlet(n)}} \right| * 100 \quad (30)$$

Table 7: Mesh refinement standard for single channel flow

Mesh Number	Number of cells	% Error P_{outlet}	%Error v_{max}	%Error T_{max}	%Error T_{avg}
1	11520	-	-	-	-
2	103680	13.5%	16.3%	0.118%	0.004%
3	198000	2.1%	2.3%	0.021%	0.002%
4	453600	1.6%	1.5%	0.017%	0.004%

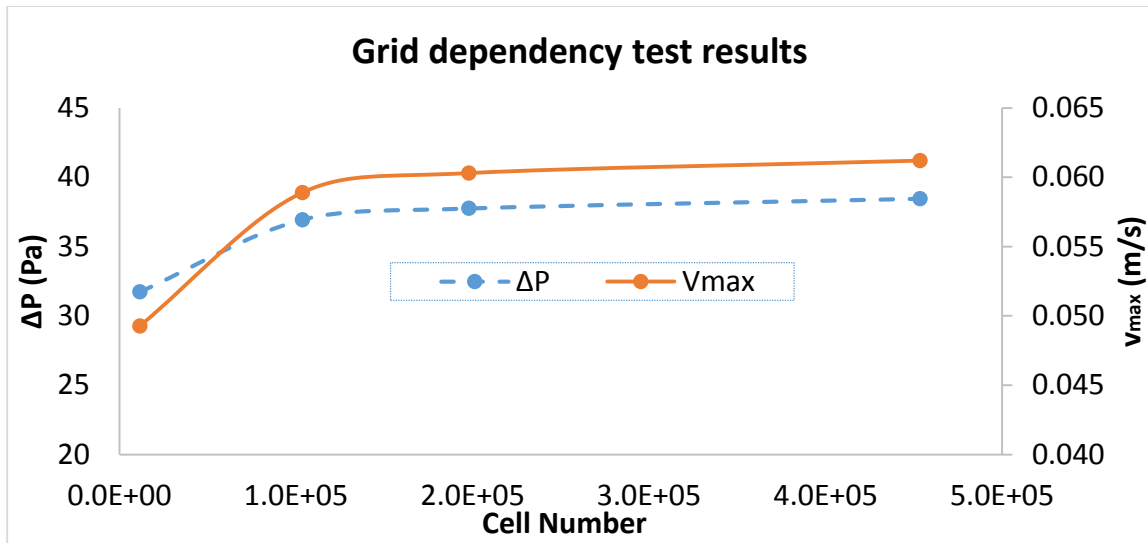


Figure 11: Grid dependency test results for single channel flow

IV.4 PIV Validation of CFD

- **Experiment setup**

The results obtained from the Particle Image Velocity (PIV) software helps understand how the fluid moves from one frame to another. It is important to do an experiment to check if the idealized boundaries definitions applied in CFD for the cooling plates are valid in reality especially at the channel wall boundary where it is assumed the fluid shear stress is zero and the flow is laminar. A diaphragm pump was used at first in the experiment to push the fluid in and out of the duct, but had to be replaced by a centrifugal pump because the flowrates obtained from the mixture with the pump weren't low enough to satisfy the targeted 30 Reynolds number in order to get the fluid's Reynolds number low enough to match the one used in ANSYS® Fluent™. Note that in the laminar boundary layer the increase Reynolds tediously increase the shear

stress. Thus doing this experiment using very low Reynolds provides more information on the interaction between fluid and channel's wall. A digital scale to measure the mass of the fluid and a graduated cylinder to measure its volume are used to find the density of the mixture composed of glycerin and water. Glycerin is added to slowly increase or the decrease the inlet flow rate just using the control valve. To find the dynamic and kinematic viscosity of the mixture a Cannon-Fenske Routine Viscometer with size 400 was used. With the viscometer constant $C_o = 1.326$ cts or mm^2s^2 , assuming a temperature of $22^\circ C$ for mixture and Efflux time, $t = 14.355s$; the fluid properties reported on the table below were obtained for kinematic viscosity, using $\vartheta = C_o t$. The efflux time is the time it takes the mixture sample to pass from the first to the second mark in the vertical position. Finally the absolute viscosity is found from the relation: $\vartheta = \mu/\rho$. Using those parameters and the senior design group code, once the targeted Reynolds was reached, the camera is positioned to start recording videos for PIV.

Table 8: Geometry and thermodynamics parameters

Fluid properties A mixture of water and glycerin	ρ	ϑ	μ
	1163.81 kg/m^3	$0.000019 \text{ m}^2/s$	0.02215 N.s/m^2
Channel geometry	H_{ch}	L_{ch}	Re_D
	0.0254 m	1.589 m	30

Table 8 shows channel size and fluid properties used to find the Reynolds number of the experiment and the camera position.

- **Experiment Procedure**

The green laser device in Figure 12 is placed on channel's length side so the laser ray pass halfway from the square channel's height. After the targeted Reynolds number was reached, acrylic particles were added into the water-glycerin mixture. The particles flowing through the duct with the mixture glow once they reach the region covered by the laser pointer. A filter was attached to the camera to enhance the visualization of the particle, for the video recording of the particle's motion which lasted an average of 10s. The flow motion is recorded in a short video using a smartphone camera as shown in Figure 12 at three different locations along the square channel. Afterwards, the video is deconstructed into multiple image frames using a GIMP software that allows for image manipulations and to modify the grayscale, brightness, and contrast of the frames to improve clarity and post processing of the output frames in the PIV app downloaded into Matlab®.

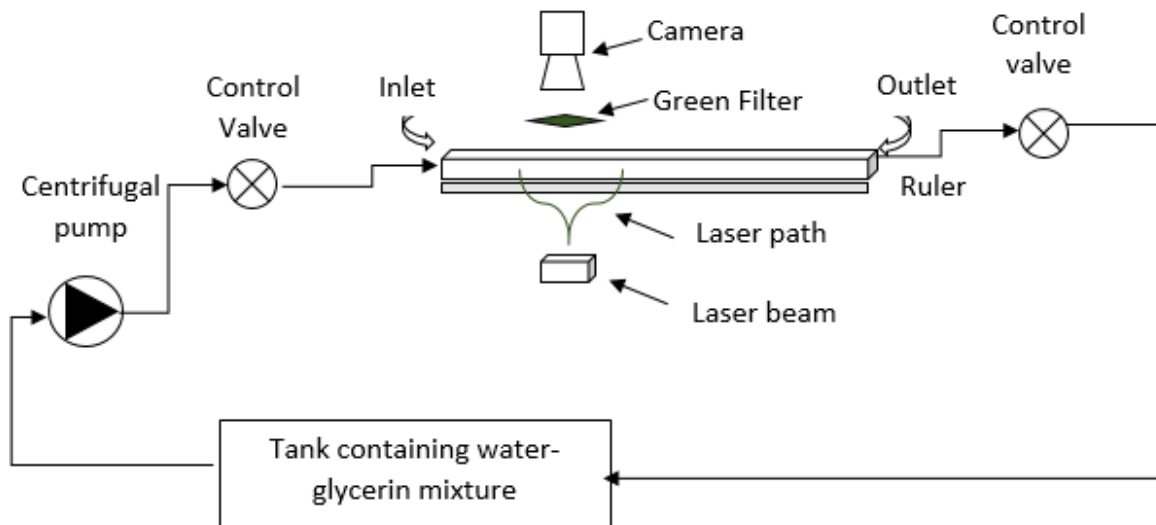


Figure 12: Schematic representation of the PIV experiment

Once in Matlab® the images treated in GIMP for each location are imported in PIV lab and analyzed and followed by vector field validation and calibration. Finally a plot of the velocity magnitude versus time is made using the data extracted from PIV.

- **CFD set up and findings**

Half of a square duct was modeled in Solidworks® software, making use of the symmetry condition at the top of the half square duct of a square duct to get the CFD results. When a half domain is simulated this way the results are the same as for a full domain (square duct). Refer to Table 9. Also, it was pointed previously that the laser was placed so that it lit the half way from the channel height. So the simulation is a correct representation of the way the experiment was set up.

Table 9: Properties comparison of Sample

Parameters	PIV	CFD
Re_D	30	30
D_h (m)	0.0254	0.0133
ρ (kgm^{-3})	1163.81	992.2
μ ($N.sm^{-2}$)	0.013	0.000653
ϑ (m^2s^{-1})	0.000012	0.00000066
\vec{v}_{in} (m/s)	0.06	0.05

The three lengths used in the experiment and defined as $L_{n(CFD)}$, where $n = 1, 2, 3$; need to be in non-dimensional in order to compare the PIV to the CFD results with the following:

$$L_n^* = \frac{L_n}{D_h} \quad (31)$$

Similarly, to plot the velocity profile of the channel the following is used:

$$x_n^* = \frac{x_n}{D_h} \quad (32)$$

Here x_n is the cross-sectional distance or channel's width. Therefore, the corresponding locations for CFD are found using the PIV non-dimensional parameters. The results are given in Table 10.

Table 10: Position Summary for non-dimensional analysis from channel inlet

$L_{(PIV)}$ Positions of Laser along channel	$L_{1(PIV)}$	$L_{2(PIV)}$	$L_{3(PIV)}$
	0.689 m	1.089 m	1.489 m
L^*	$L_{1(PIV)}^*$	$L_{2(PIV)}^*$	$L_{3(PIV)}^*$
	27.1	42.9	58.6
$L_{(CFD)}$ Positions of planes channel	$L_{1(CFD)}$	$L_{2(CFD)}$	$L_{3(CFD)}$
	0.036 m	0.057 m	0.078 m

Even though the location were different the CFD velocities kept the same profile at the three locations. That is because the fluid was already fully developed in those regions. PIV results are shown in Appendix D. From these outputs and keeping in mind that the CFD velocity profile (Appendix C-2) was the same at the three different locations a comparative plot combining CFD and PIV was done at the 2nd location for both because that is the location that had PIVlab was able to compute data close to the channel walls.

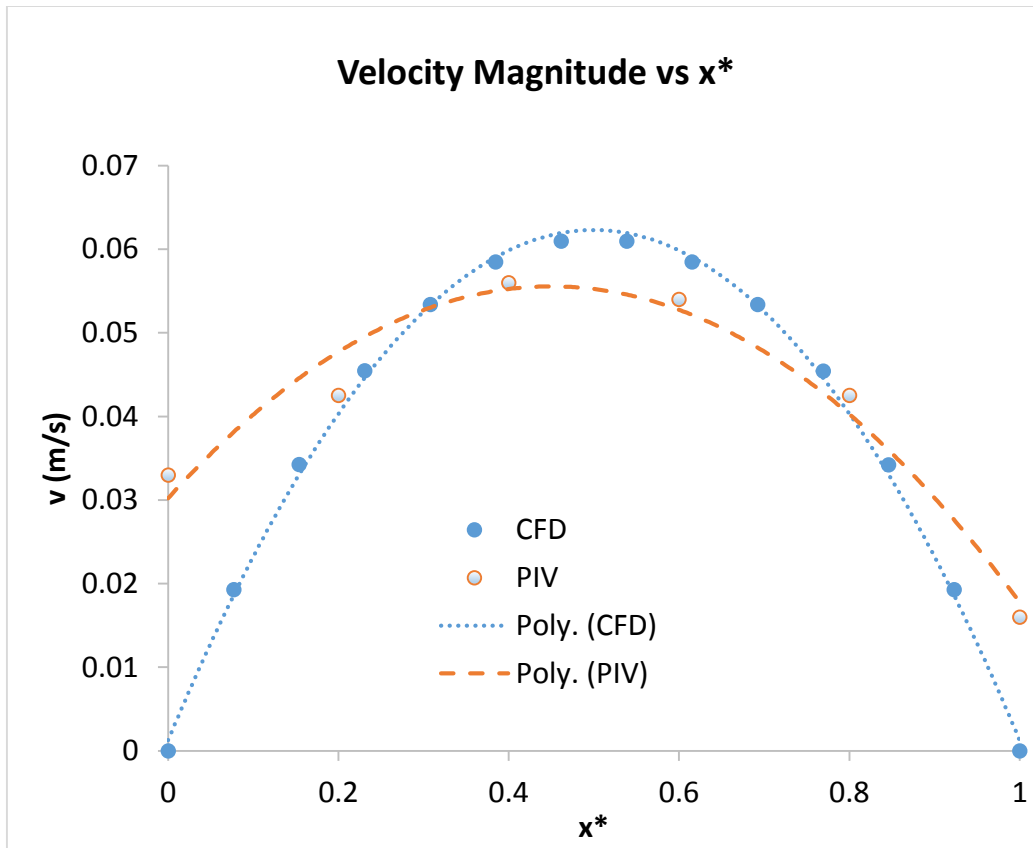


Figure 13: comparative result for the velocity profile obtained between PIV experiment and CFD simulation

The plot of Figure 13 shows that CFD correlates with PIV for the velocity profile. The PIV data at locations 1 and 3 could not generate data near the edge because near the walls the light gets reflected and shines brighter than the particles flowing in the wall region. Also the PIV results display that the non-slip condition near the walls is more difficult to achieve in reality but we conclude that by increasing the inlet velocity that error can be reduced.

Chapter V. COOLING PLATE RESULTS AND ANALYSIS

V.1 Temperature and Velocity Outputs Comparison

- Temperature distribution

ANSYS® Fluent™ results for temperature are shown in figure 14. under specified geometry and boundary conditions mentioned in this report. To validate the set up and CFD calculations in terms of thermal management analysis the fluid static temperature profile are obtained from Fluent, refer to figures 14-c CPFF and and 14-b from SFF and compared to the ones shown in [6], refer to 14-a and14-b.

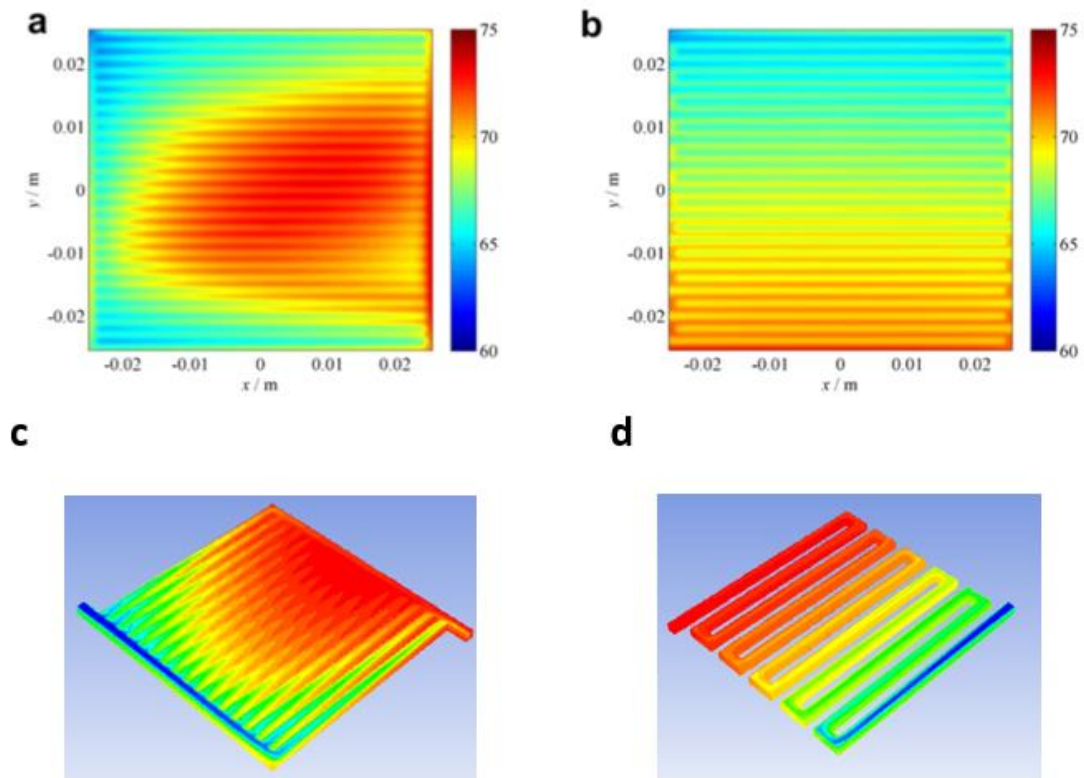


Figure 14: Temperature distribution from published (a-b) vs current CPFF (c) and SFF (d) temperature distribution

- Finding \overline{Nu} and U

Equations 23 and 24 are used to find the mean temperature to be used to calculate the Nusselt number from Equation 25. Central difference is more precise than forward difference computations, but doesn't project results at the end points thus the forward difference was carried out to produce the Nusselt number values shown in the plot summarizing the findings below.

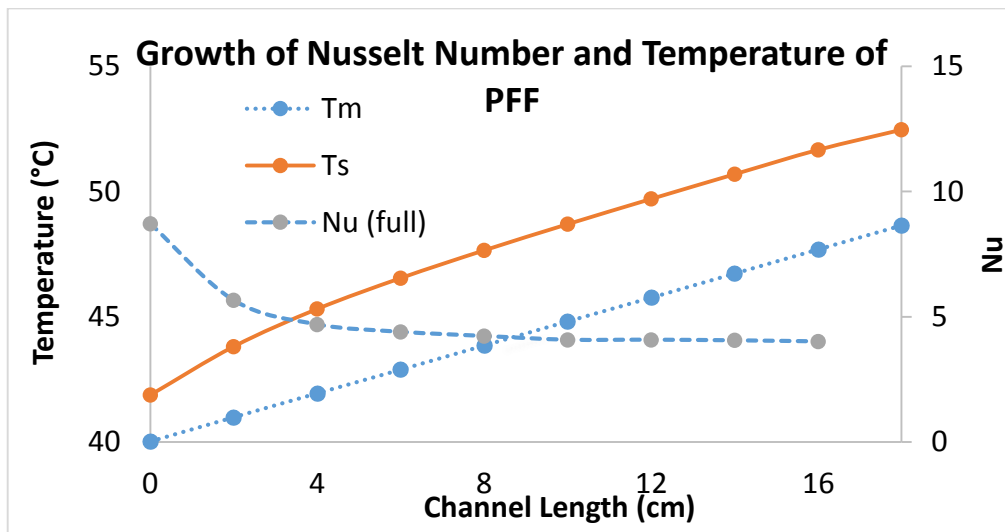


Figure 15: Current parallel straight channels heat transfer characteristics

From Figure 15, the shape of the plot matches that obtained by Baek [7]. On the article The Nusselt number converged to $Nu = 5.7$ while the accepted value in the references was $Nu = 4.13$. Our results have shown to converge to $Nu = 4.01$ which is much closer to the accepted value with a 3% Error compared to a 38 % error in the published results. Similarly, in Figure 16 results the Darcy friction factor times the Reynolds number converged to $fRe_D = 61.9$ in this analysis compared with 59.7 obtained from the published results. The accepted value was referred in the article to be 62 for a

rectangular channel which gives the present results a 0.16% Error compared to 3.7% Error from previous research.

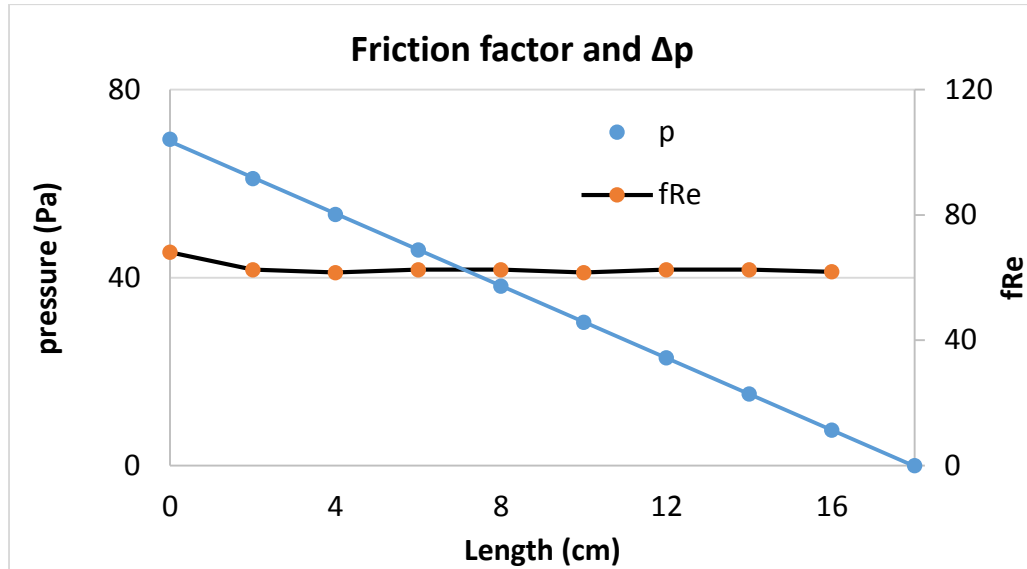


Figure 16: Pressure distribution and Darcy friction factor along PFF channel length

The data comparison is a success but not a perfect match to the data found in [7].

Looking at the temperature variation and pressure drop shown in Figures 15 and 16 respectively, for a SFF design it is clear that fRe_D quickly converges to 62 as expected for this flow with the assigned boundary conditions.

It validates the heat transfer results that will follow. Since the mean temperature values are used to plot Figure 15, they will be used to compute the overall heat transfer from the Nusselt number and the effectiveness of the heat transfer between graphite plate and cooling water with the following equalities:

$$\epsilon = \frac{\dot{Q}_{act}}{\dot{Q}_{max}} \quad (33)$$

$$\dot{Q}_{act} = \dot{m}c_p(T_{out} - T_{in}) \quad (34)$$

$$\dot{Q}_{max} = \dot{m}c_p(T_{s,in} - T_{f,in}) \quad (35)$$

$$UA = (q''A)/(T_{out} - T_{in}) \quad (36)$$

Varying the Reynolds number in the plate produced the output shown in Figure 17. It is observed that as the efficiency converges to the Reynolds at around 75% of operations of the cooling plates. Most cooling plate designs are about 60% efficient so those results demonstrates the assigned boundary conditions to be reliable and therefore moving to the second part of the analysis which is the creation of data from entropy generation rates.

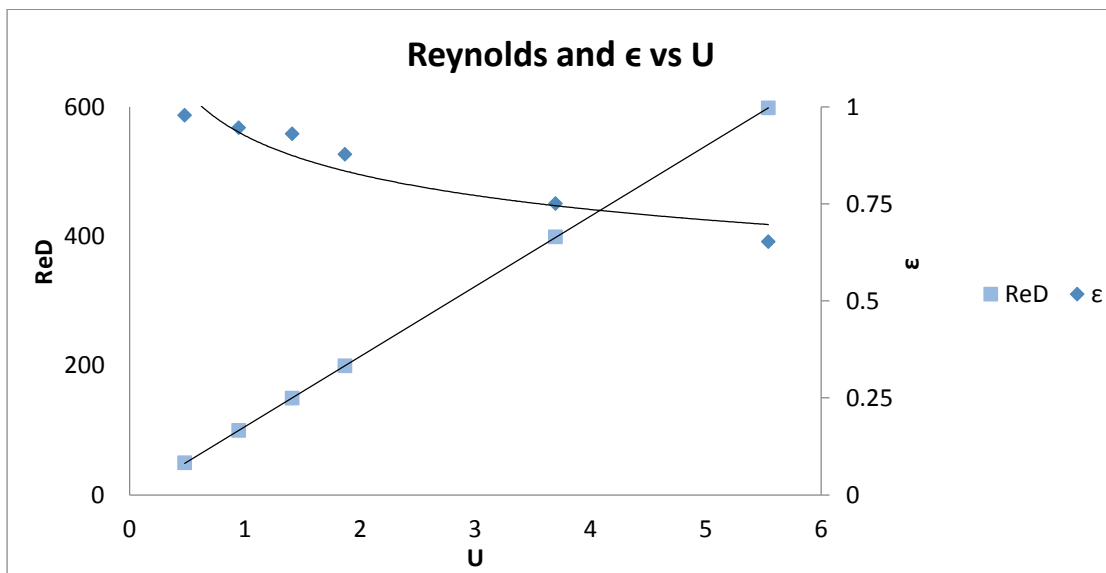


Figure 17: Reynolds number and Efficiency with respect to the Overall heat transfer in PFF

- Velocity effects on different cooling plate

Table 11: Geometry specifications

Geometry	SFF	CPFF
Channels (length-width in mm)	42 (175-2)	45(180)
Connections (length-width in mm)	41 (2-2)	2 (180-2)
Inlet extension	1 (102.5-2)	1 (99-2)
Outlet extension	1 (107-2)	1 (99-2)

Figure 18 shows the difference between inlet and outlet temperatures by varying inlet velocities measured in volume flow rates for SFF and CPFF designs.

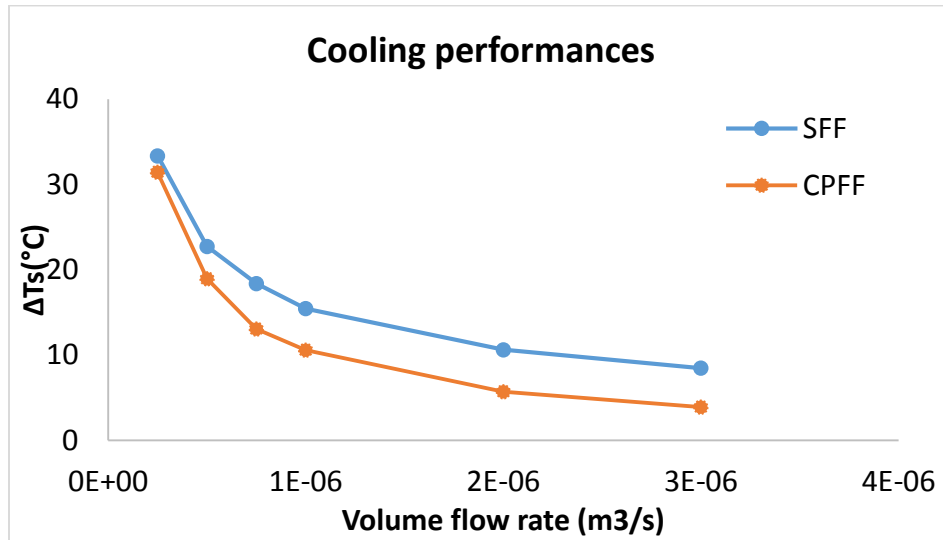


Figure 18: Plates performance with modified flow field designs

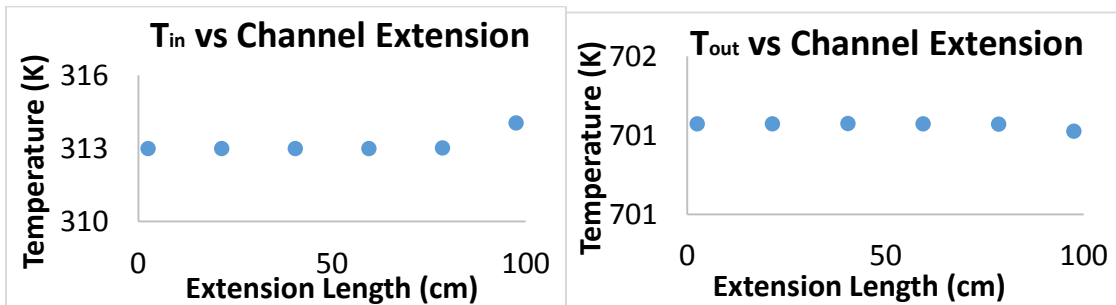


Figure 19: Temperature Inlet/outlet data along SFF extensions

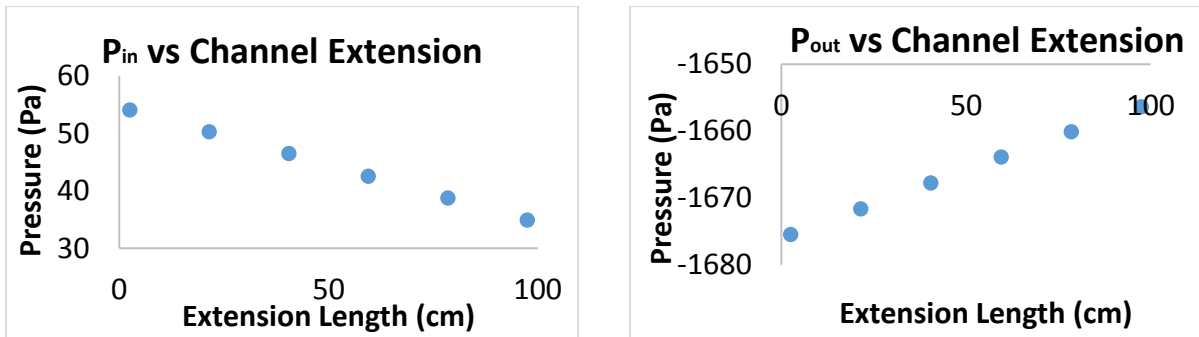


Figure 20: Pressure Inlet/outlet data along SFF extensions

Adding extensions (Refer to Table 11) to the designs ensures the outflow condition was respected. It leads us to notice that there is no need for extensions in CFD. As Figure 19 illustrates, the temperature at the extension which begins at the inlet stays constant until it reaches the section of the cooling plate where the heat flux is applied. In Figure 20 pressure decreases linearly as expected along inlet extension. The outlet extensions that shows similarities as seen in the inlet except that the temperature it begins where the cooling fluid exit the heated plate. The temperature also stays constant and only fluctuates as it reaches the end of the extension boundary. The next set of computation can therefore be carried out without extensions and just looking at the mass flow rates from inlet to outlet. The temperatures are high because the pressure drop is not high enough so that the water is not evaporating. This is due to assigned inlet velocities set at 0.05 m/s. For results applicable to PEMFC the inlet velocities were changed for SFF and PFF designs without extensions after it had been established that having extensions at the inlet and outlet did not impact data from simulation.

V.2 Local \dot{S}_{gen} Analysis

- Entropy generation \dot{S}_{gen}

Table 12: Difference in total entropy using SLT and mesh information

Designs	Number of cells	$\dot{S}_{gen} (WK^{-1})$	Sets	% Difference
PFF	22,122,014	0.00611	SFF vs PFF	34.81%
SFF	8,100,000	0.008684	CPFF vs SFF	38.08%
CPFF	21,063,395	0.012769	CPFF vs PFF	70.55%

The volumetric analysis of the cooling plate carried using SLT (Equation 20) to account for the frictional and thermal irreversible thermodynamic processes are computed at different locations from channel height using CFD in different cooling plate designs (refer to Figures 3, 4 and 5) It is shown that the entropy production in the cooling plate was considerably higher in CPFF Refer to Table 12. The PFF had the lowest entropy rate. However, SFF and CPFF designs have different Reynolds compared to PFF designs because they both have one inlet and one outlet. Thus, comparing SFF and CPFF, SFF had a lower entropy generation which correlates with previous research findings stating that serpentine is a better design compared to combined parallel channel designs. The volume integration of the entropy generation found in CFD is used to compute the performance chart shown below.

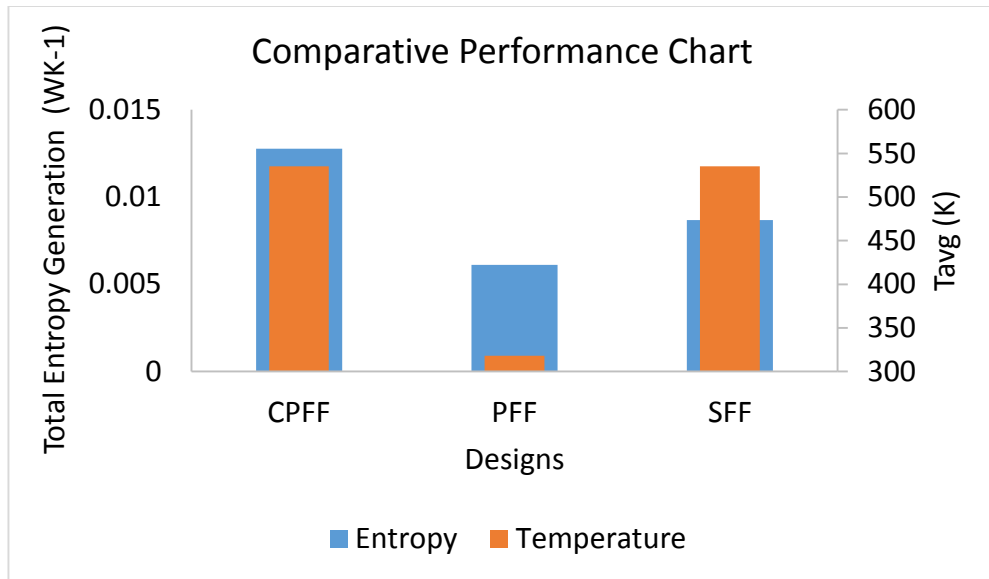


Figure 21: Volumetric entropy and temperature variations from each model

Graphical results (Refer to Appendix E) show the thermal dependence of the entropy for all the designs. For PFF and CPFF designs the variations are happening close to the inlet region of the fluid interior. While the SFF show changes in entropy throughout the cooling plates. This could be because that design has multiple inlets therefore multiple regions where the entropy in both thermal and frictional can develop. Thus increasing the number of channel inlets will increase the entropy of a model. The pressure drop from both CPFF and SFF are very different. From Figure 22 CPFF has higher pressure drops compared to PFF.

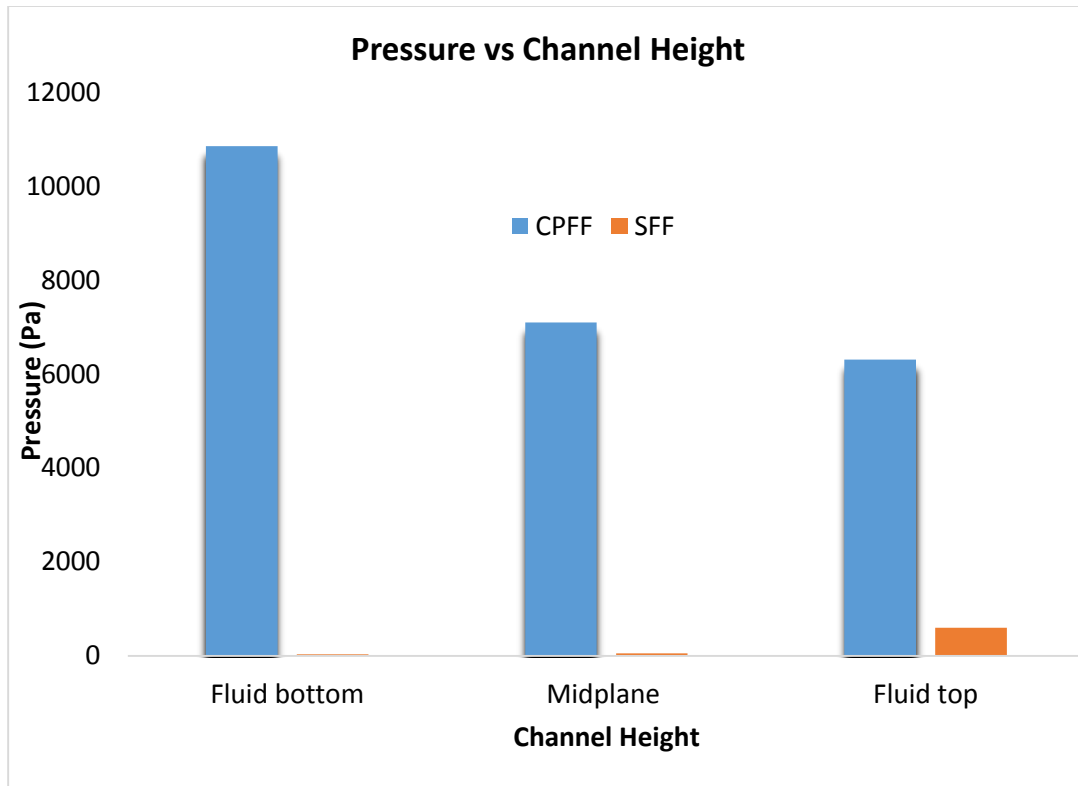


Figure 22: Performance chart based on pressure drop

V.3 Summary Tables and Figures

Table 13: Results Summary by method of Analysis

Method	Velocity profile	Temperature profile	Entropy generation
Fluent	YES	YES	Yes
PIV experiment	YES	NO	NO

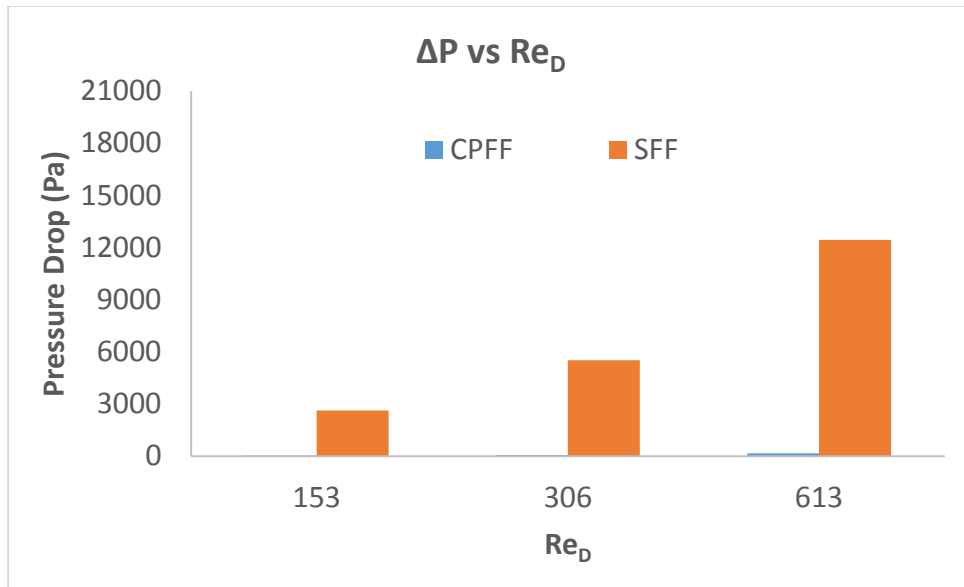


Figure 23: Pressure drop of the coolant from inlet to outlet of SFF and CPFF designs when varying the Reynolds number

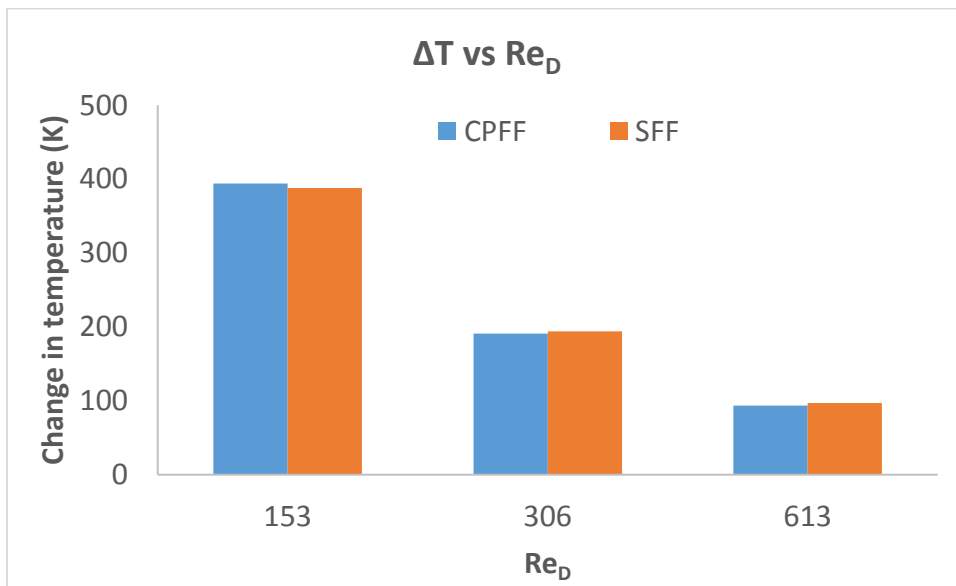


Figure 24: Temperature increase of the coolant from inlet to outlet of SFF and CPFF designs at different Reynolds number

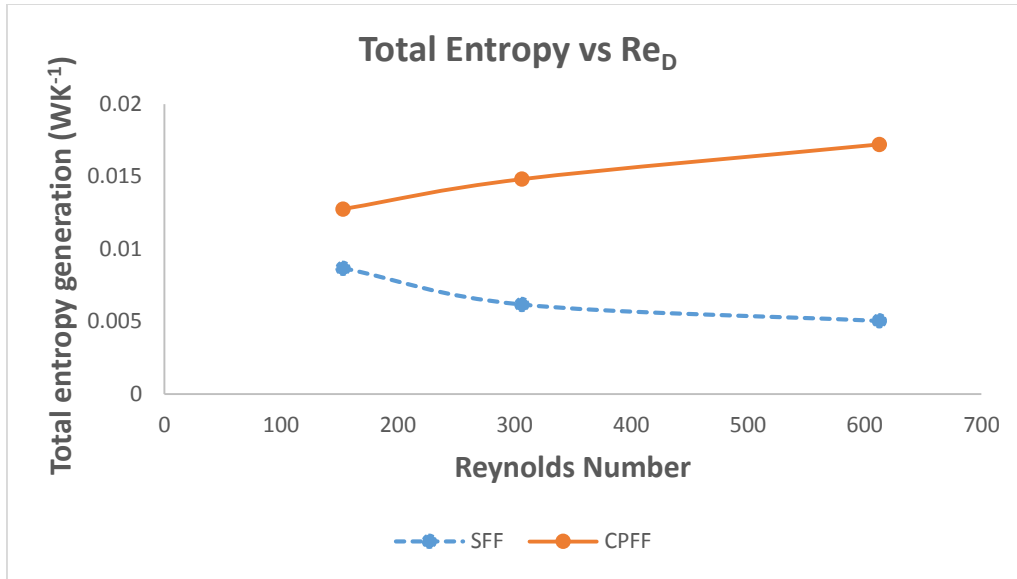


Figure 25: Volume integral of the entropy generated in the coolant when varying the inlet velocity for SFF and CPFF designs.

Table 14: Current data obtained for the frictional and thermal components of the total entropy generation in the coolant

v (m/s)	CPFF		SFF	
	\dot{S}_{gen} from cooling plates (WK^{-1})			
	Thermal	Friction	Thermal	Friction
0.05	1.3E-02	7.8E-09	8.7E-03	5.2E-07
0.10	1.5E-02	3.8E-08	6.2E-03	2.7E-06
0.20	1.7E-02	1.8E-07	5.1E-03	1.3E-05

Chapter VI. CONCLUSION

PEMFC performance is attributed to the cell components and operating conditions. A CFD study focused on the internal heat transfer was carried out on cooling plates with various geometries. Entropy generation was computer-generated based on SLT. The local volumetric results was found to have a noteworthy effect on the temperature distribution. The temperature changes measured with the temperature gradients under extreme conditons on the cooling plate were higher that the measured heat dissipation from friction in all designs. Those results were expected for CPFF and SFF because of the assigned inlet velocity, but surprising for the PFF which oly had an increase in temperature of 48°C from the inlet temperature set at 40°C in all models. This suggest that temperature gradients take ove in the entropy generation which negatively impact on the internal resistance of a PEMFC satck. The SLT method shown is functional to cell design and performance. Further study should focus on the overall heat exchanger performance.

The first implication on this study involves the size of the mesh. SFF designs simulations were carried over 8 million cells compared to 4.2 million cells in the literature. The adjustment helped to get values of Nusselt Number and Darcy friction factor closer to the accepted values for a rectangular channel. Table 8 showing mesh refinements results helps to notice that looking at the variations in pressures and velocities compared to the variations in temperature will increase the accuracy of the simulation. At the same time it increases the mesh size required to perform CFD and this

can be very challenging when considering bipolar plates of a larger size. That is to say the ANSYS® Fluent™ software will experience a very slow development which requires the use of supercomputers to maximize output speed and reduce simulation time.

The second implication involves the SLT method which when looking at the entrance region helps identifying where the thermal and hydrodynamic boundary layers occur. This means that one can be sure to notice regions where the fluid is fully developed, particularly for the SFF designs where the fluids makes multiple passes, SLT analysis shows how the entropy changes from one pass the other. It is determined based on the SLT method that the corners of the cooling plate need to be smooth in order to reduce the entropy generation. The sharp corners have the highest recorded entropy and this is due to the fluid contact region with the solid decreasing at these locations. Also, smoother edges along the channels with produce better heat transfer from fluid to solid interactions.

Appendix A:
List of References

[1] Woodward, Alistair et al. Climate change and health: on the latest IPCC report. *The Lancet*, Volume 383, Issue 9924, 1185 - 1189

[2] Mavrotas, G., Gakis, N., Skoulaxinou, S., Katsouros, V., & Georgopoulou, E. (2015). Municipal solid waste management and energy production: Consideration of external cost through multi-objective optimization and its effect on waste-to-energy solutions. *Renewable and Sustainable Energy Reviews*, 51, 1205-1222.

[3] Bright, A. (2010). Renovating American Infrastructure, Step 5: Sewage. *Popular Science*.

[4] Mercer, J. (2012). Microbial Fuel Cells: Generating Power from Waste. *Illumin*. (online) <http://illuminate.usc.edu/134/microbial-fuel-cells-generating-power-from-waste/>

[5] Wang, Y., Chen, K. S., Mishler, J., Cho, S. C., & Adroher, X. C. (2011). A review of polymer electrolyte membrane fuel cells: technology, applications, and needs on fundamental research. *Applied Energy*, 88(4), 981-1007.

[6] Sasmito, A. P., Kurnia, J. C., & Mujumdar, A. S. (2012). Numerical evaluation of various gas and coolant channel designs for high performance liquid-cooled proton exchange membrane fuel cell stacks. *Energy*, 44(1), 278-291. doi:10.1016/j.energy.2012.06.030

[7] Baek, S. M., Yu, S. H., Nam, J. H., & Kim, C. J. (2011). A numerical study on uniform cooling of large-scale PEMFCs with different coolant flow field designs. *Applied Thermal Engineering*, 31(8), 1427-1434.

[8] Sasmito, A. P., Birgersson, E., & Mujumdar, A. S. (2011). Numerical investigation of liquid water cooling for a proton exchange membrane fuel cell stack. *Heat Transfer Engineering*, 32(2), 151-167. doi:10.1080/01457631003769302

[9] Ray, D. R., Das, D. K., & Vajjha, R. S. (2014). Experimental and numerical investigations of nanofluids performance in a compact minichannel plate heat exchanger. *International Journal of Heat and Mass Transfer*, 71, 732-746.

[10] Ramos-Alvarado, B., Li, P., Liu, H., & Hernandez-Guerrero, A. (2011). CFD study of liquid-cooled heat sinks with microchannel flow field configurations for electronics, fuel cells, and concentrated solar cells. *Applied Thermal Engineering*, 31(14), 2494-2507.

[11] Gould, B. D., Ramamurti, R., Osland, C. R., & Swider-Lyons, K. E. (2014). Assessing fuel-cell coolant flow fields with numerical models and infrared thermography. *International journal of hydrogen energy*, 39(26), 14061-14070.

[12] Li, X., & Sabir, I. (2005). Review of bipolar plates in PEM fuel cells: Flow-field designs. *International Journal of Hydrogen Energy*, 30(4), 359-371.

[13] Heidary, H., Abbassi, A., & Kermani, M. J. (2013). Enhanced heat transfer with corrugated flow channel in anode side of direct methanol fuel cells. *Energy Conversion and Management*, 75, 748-760.

[14] Lasbet, Y., Auvity, B., Castelain, C., & Peerhossaini, H. (2007). Thermal and hydrodynamic performances of chaotic mini-channel: application to the fuel cell cooling. *Heat Transfer Engineering*, 28(8-9), 795-803.

[15] Nikam, V. V., & Reddy, R. G. (2006). Corrugated bipolar sheets as fuel distributors in PEMFC. *International journal of hydrogen energy*, 31(13), 1863-1873.

[16] Arsenyeva, O., Kapustenko, P., Tovazhnyansky, L., & Khavin, G. (2013). The influence of plate corrugations geometry on plate heat exchanger performance in specified process conditions. *Energy*, 57, 201-207.

[17] Stogiannis, I. A., Mouza, A. A., & Paras, S. V. (2013). Study of a micro-structured PHE for the thermal management of a fuel cell. *Applied Thermal Engineering*, 59(1), 717-724.

[18] Xuedong, L., Hanpeng, L., & Ling, Z. Numerical Simulation of Heat Transfer in Primary Surface with Corrugations Recuperators.

[19] WAN, W. M. (2012). Analysis of excessive heating on the thermal and electrical resistance of a polymer electrolyte membrane fuel cell. *International Journal of Automotive and Mechanical Engineering (IJAME)*, 5, 648-659.

[20] Ravishankar, S., & Prakash, K. A. (2014). Numerical studies on thermal performance of novel cooling plate designs in polymer electrolyte membrane fuel cell stacks. *Applied Thermal Engineering*, 66(1), 239-251.

[21] Zhang, G., & Kandlikar, S. G. (2012). A critical review of cooling techniques in proton exchange membrane fuel cell stacks. *International Journal of Hydrogen Energy*, 37(3), 2412-2429.

[22] O'Keefe, D., El-Sharkh, M. Y., Telotte, J. C., & Palanki, S. (2014). Temperature dynamics and control of a water-cooled fuel cell stack. *Journal of Power Sources*, 256, 470-478. doi:10.1016/j.jpowsour.2013.12.100

[23] Mohamed, W., Atan, R., & Ismail, A. A. (2010, December). Heat transfer simulation of a single channel air-cooled Polymer Electrolyte Membrane fuel cell stack with extended cooling surface. In *Science and Social Research (CSSR), 2010 International Conference on* (pp. 91-96). IEEE.

[24] Soupremanien, U., Le Person, S., Favre-Marinet, M., & Bultel, Y. (2012). Tools for designing the cooling system of a proton exchange membrane fuel cell. *Applied Thermal Engineering*, 40, 161-173.

[25] Lopez-Sabiron, A. M., Barroso, J., Roda, V., Barranco, J., Lozano, A., & Barreras, F. (2012). Design and development of the cooling system of a 2 kW nominal power open-cathode polymer electrolyte fuel cell stack. *International Journal of Hydrogen Energy*, 37(8), 7289-7298.

[26] Akbari, M., Tamayol, A., & Bahrami, M. (2012). Thermal assessment of convective heat transfer in air-cooled PEMFC stacks: an experimental study. *Energy Procedia*, 29, 1-11.

[27] Rangel-Hernandez, V. H., Damian-Ascencio, C., Juarez-Robles, D., Gallegos-Muñoz, A., Zaleta-Aguilar, A., & Plascencia-Mora, H. (2011). Entropy generation analysis of a proton exchange membrane fuel cell (PEMFC) with a fermat spiral as a flow distributor. *Energy*, 36(8), 4864-4870.

[28] Oztop, H. F., & Al-Salem, K. (2012). A review on entropy generation in natural and mixed convection heat transfer for energy systems. *Renewable and Sustainable Energy Reviews*, 16(1), 911-920.

[29] Stogiannis, I. A., Mouza, A. A., & Paras, S. V. (2013). Study of a micro-structured PHE for the thermal management of a fuel cell. *Journal of Applied Thermal Engineering*, 59(1), 717-724.

[30] Reddy, E. H., Monder, D. S., & Jayanti, S. (2013). Parametric study of an external coolant system for a high temperature polymer electrolyte membrane fuel cell. *Applied Thermal Engineering*, 58(1), 155-164.

[31] Senn, S. M., & Poulikakos, D. (2004). Laminar mixing, heat transfer and pressure drop in tree-like microchannel nets and their application for thermal management in polymer electrolyte fuel cells. *Journal of Power Sources*, 130(1), 178-191.

[32] (2007). Heat transfer and entropy generation optimization of forced convection in porous-saturated ducts of rectangular cross-section. *International Journal of Heat and Mass Transfer*. 50, 2051–2059.

Appendix B:
Setting up Mesh Interface

ANSYS® Fluent™ will not be able to perform iterations. Another technique involves defining just one interface at the solid boundary that connects both the solid and fluid part but this has been proven to work easily in cases when the contact region between the solid and fluid has one surface, like that of fluid going through a smooth pipe. The interface has only one face but in this case study the interface have multiple faces. New walls will be created in fluent. Wall 4 and wall 4 shadow, created in interface region shown in figure 10, represent the solid and the fluid interface zones respectively, are coupled in fluent to satisfy heat transfer condition at the interface between the solid and fluid part to transform them as one interface. Wall 15 and wall 16 represent the wall boundary zones that are created in addition to wall4 and wall 4 shadow because the solid and fluid interfaces are connected with each other and therefore share the same surface. Wall 15 and 16 do not represent actual faces but exist as a consequence of the solid and fluid interface name selection. After convergence of simulation by assigned residuals, and to verify the assumptions made in the boundary conditions, the area source (src) and target (trg) were compared to wall 4 and wall 4 shadow in Table 14.

Table 15: Area comparison of the interfaces created in fluent versus interface zones wall 4 and wall 4 shadow

Boundary conditions at the fluid/solid interfaces	Area (m ²)
solid_interface-contact_region-src	0.0297479
fluid_interface-contact_region-trg	0.0297479
wall-4	0.0297479
wall-4-shadow	0.0297479

Appendix C: Setting up Fluent

Appendix C-1

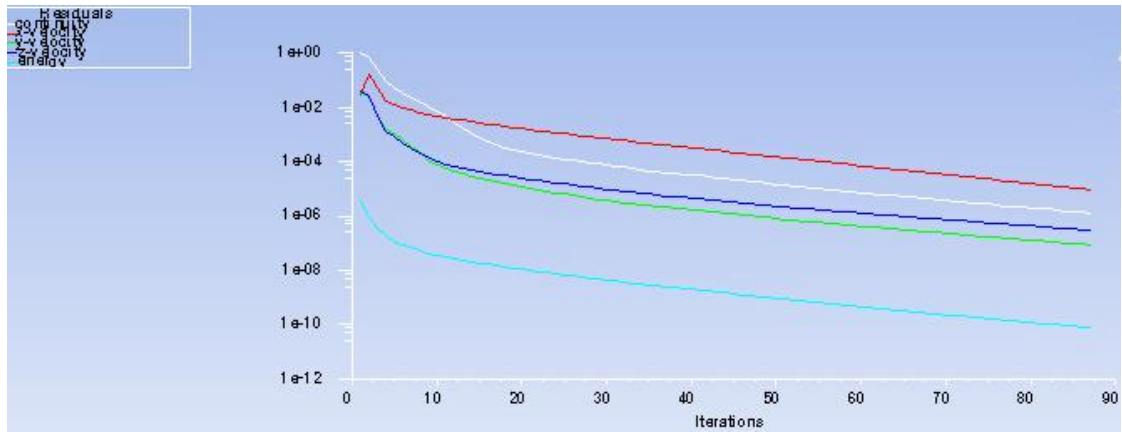


Figure 26: Single straight channel 4th Mesh Residuals

The stopping factor was set at 10^{-5} for continuity, velocities in all 3 directions (x, y and z), and energy in ANSYS® Fluent™.

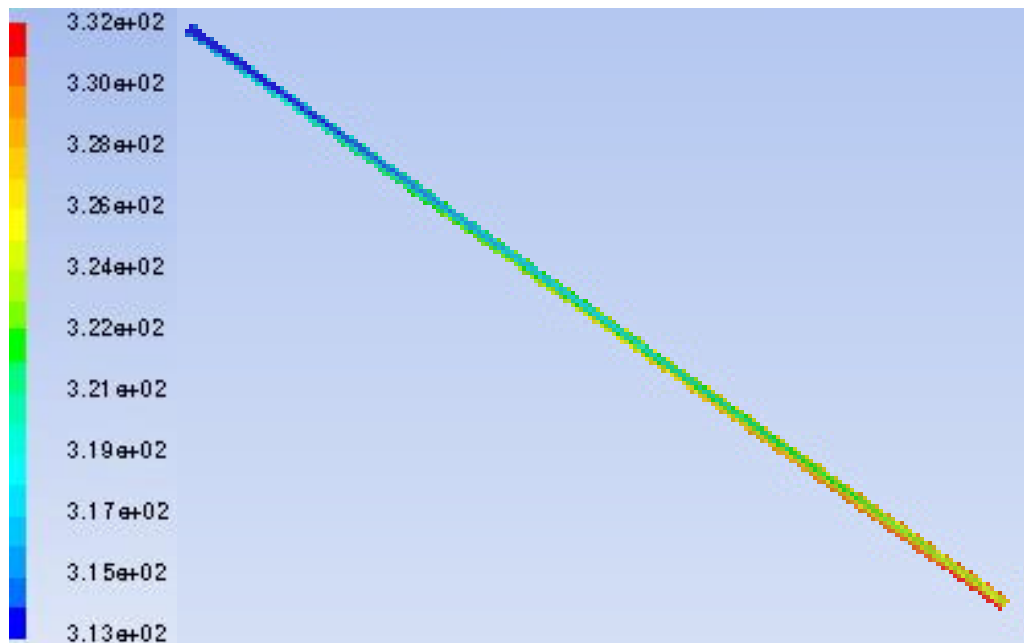


Figure 27 Single straight channel 4th Mesh graphical Contours of Static Temperature (K) of the fluid interior in ANSYS® Fluent™

Appendix C-2

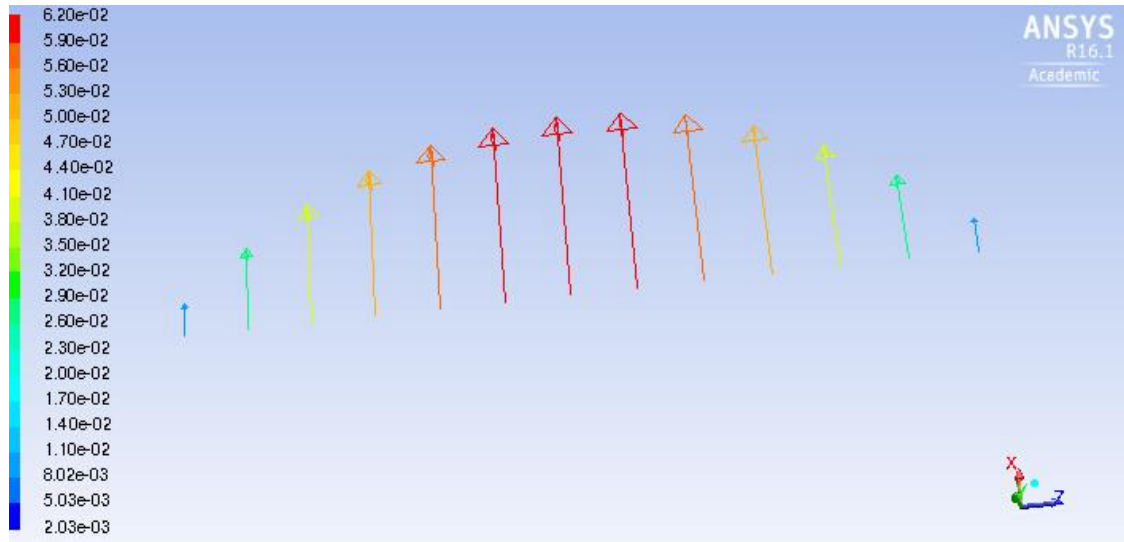


Figure 28: Single straight channel 4th Mesh Velocity Vector of Velocity Magnitude (m/s) of the top fluid surface where the symmetry boundary was applied in ANSYS® Fluent™

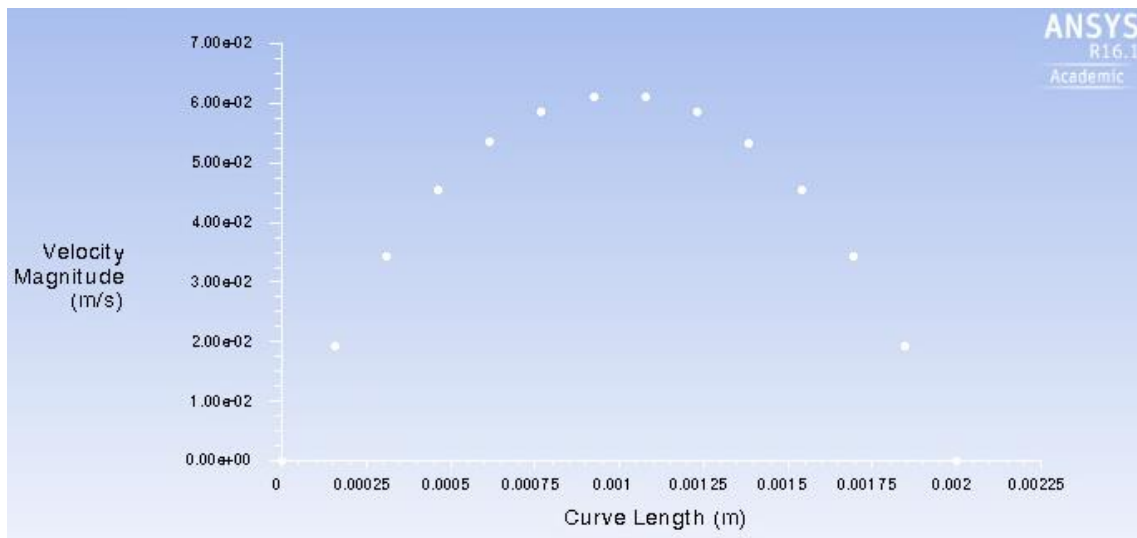
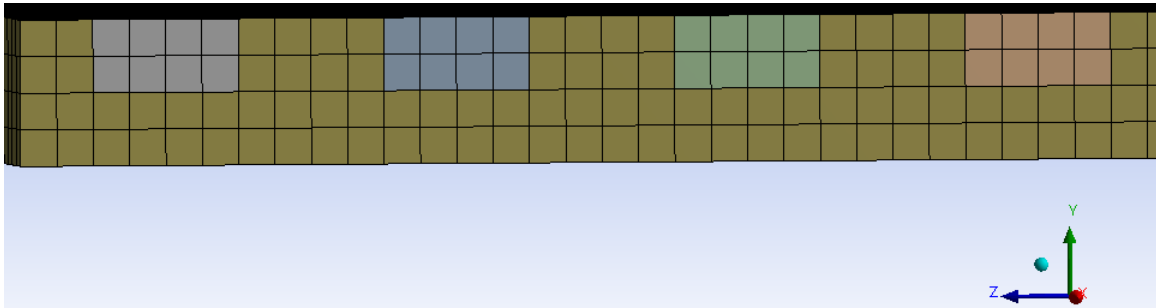


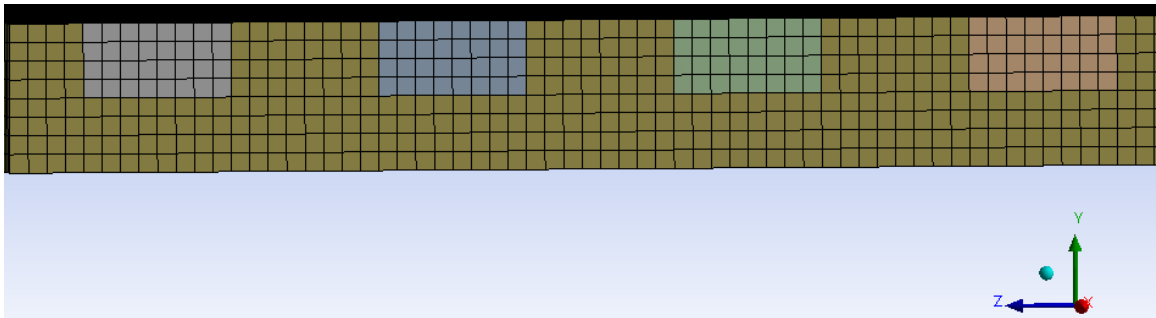
Figure 29: Single straight channel 4th Mesh Plot of Velocity Magnitude vs channel width (curve length) at the top fluid surface in ANSYS® Fluent™

Appendix C-3

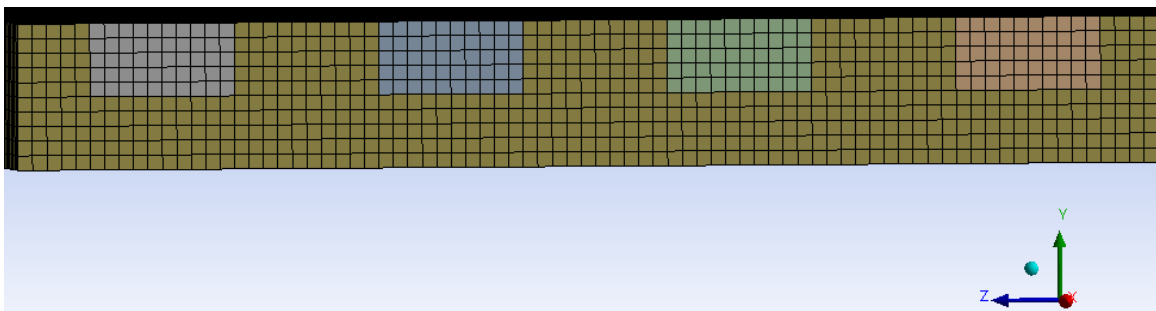
45 PFF mesh refinement in ANSYS® Workbench™.



1st Mesh



2nd Mesh



3rd Mesh

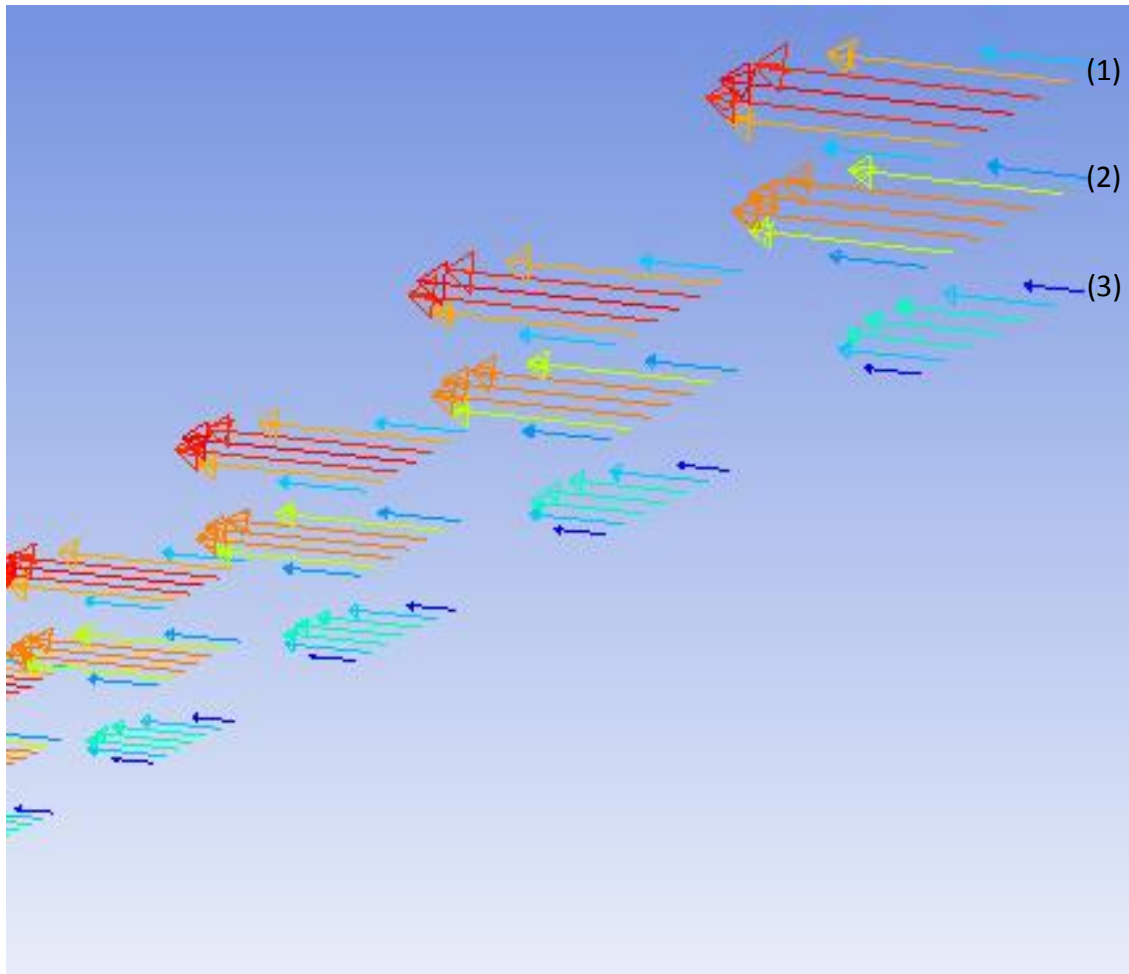


Figure 30: PFF 3rd Mesh Velocity Vectors represented by magnitude

45 Straight Parallel Channels 3rd Mesh Velocity Vectors of Velocity Magnitude (m/s) of the top fluid surface (1), halfway through channel height (2), and bottom fluid surface (3) in ANSYS® Fluent™.

Appendix D:
PIV Lab Results

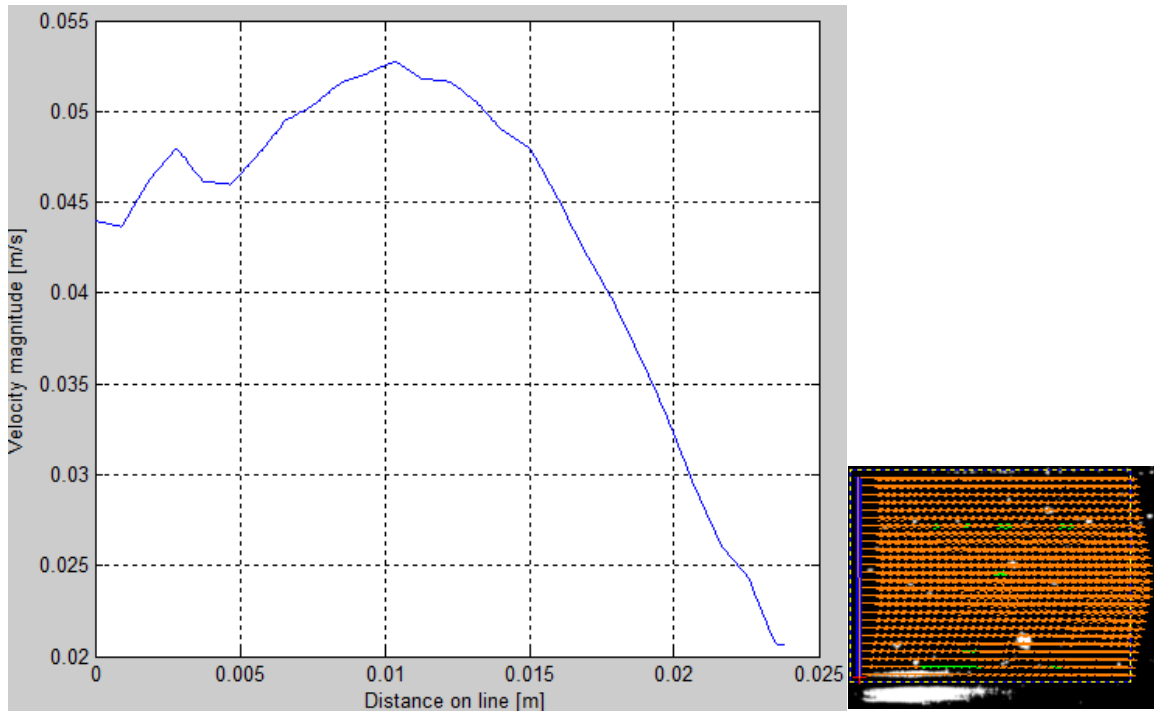


Figure 31: PIV at $L_1(\text{PIV})$

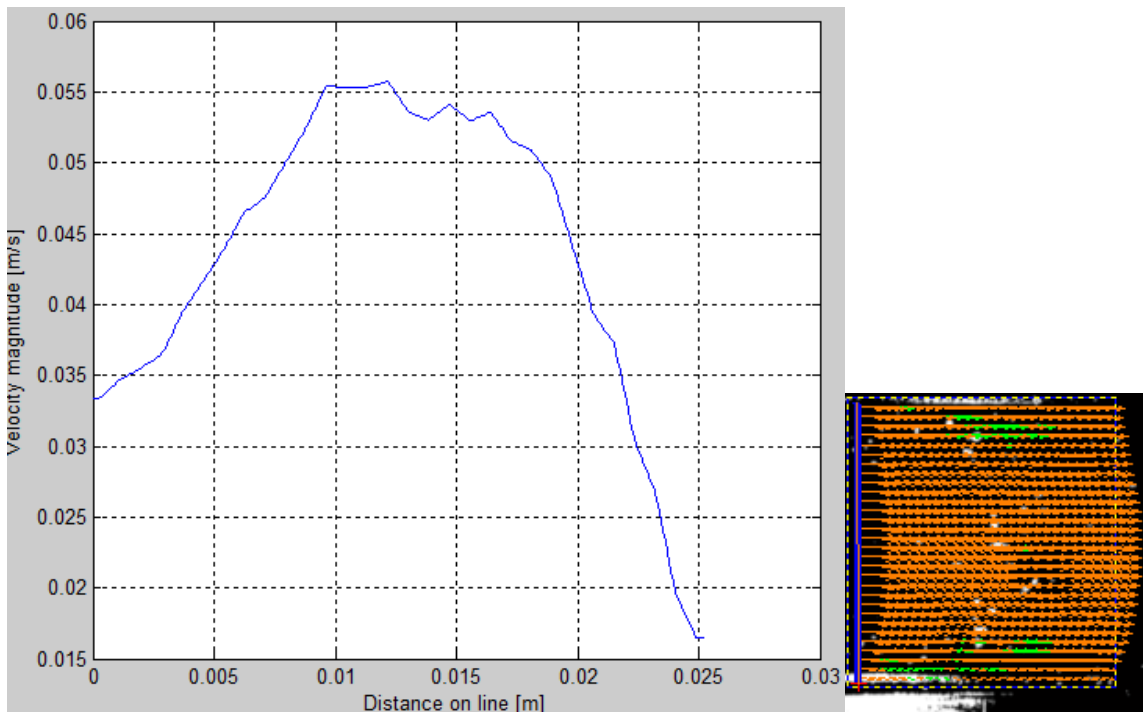


Figure 32: PIV at $L_2(\text{PIV})$

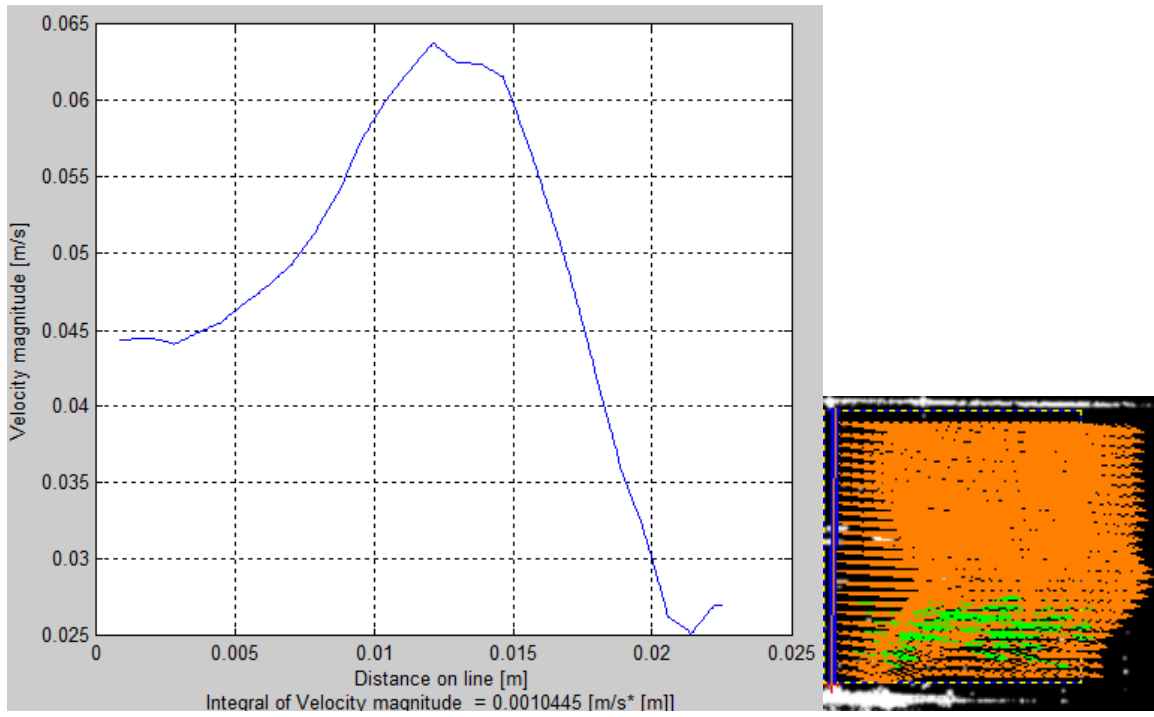


Figure 33: PIV at $L_{3(PIV)}$

Appendix E:
Cooling Plate Graphical Results

Appendix E-1: CFFF Results

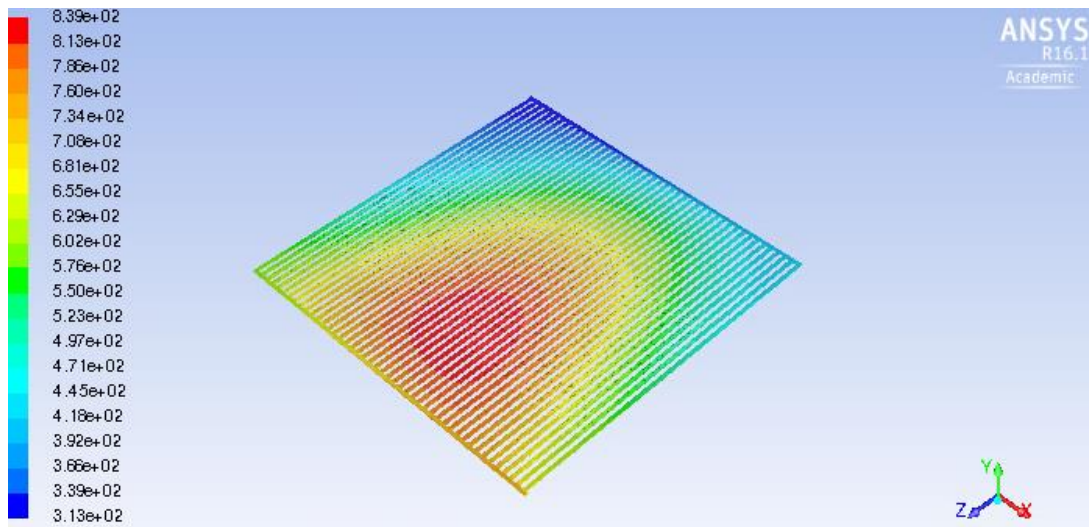


Figure 34: Contours of the temperature distribution with an inlet velocity of 0.05 m/s

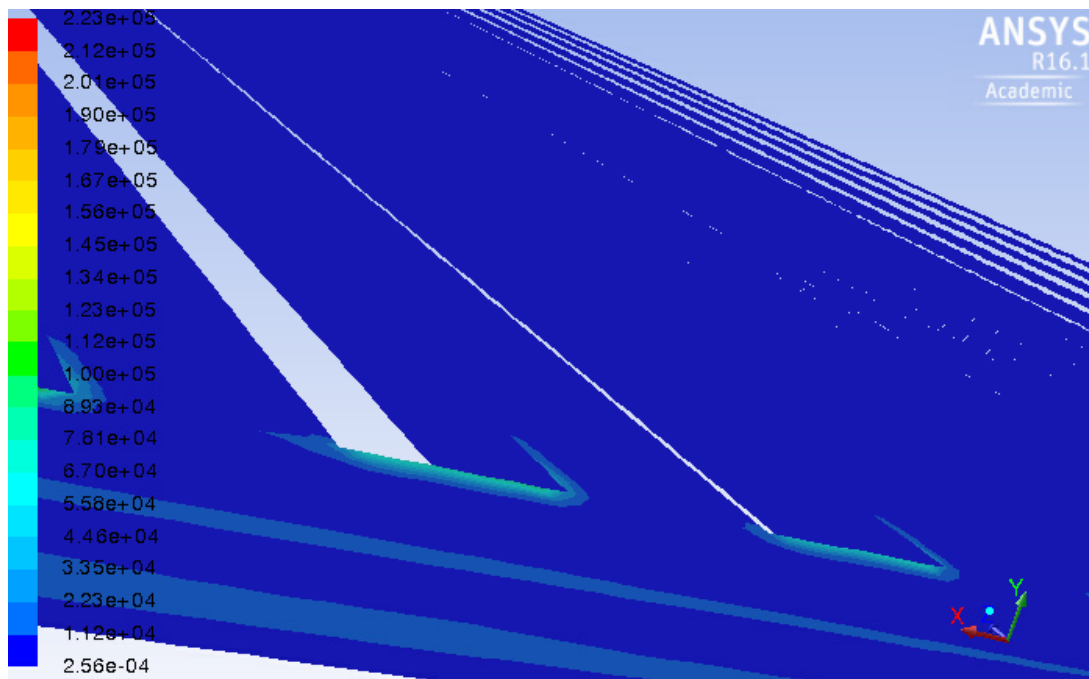


Figure 35: Contours of the volume integral of entropy at the inlet region with an inlet velocity of 0.05 m/s

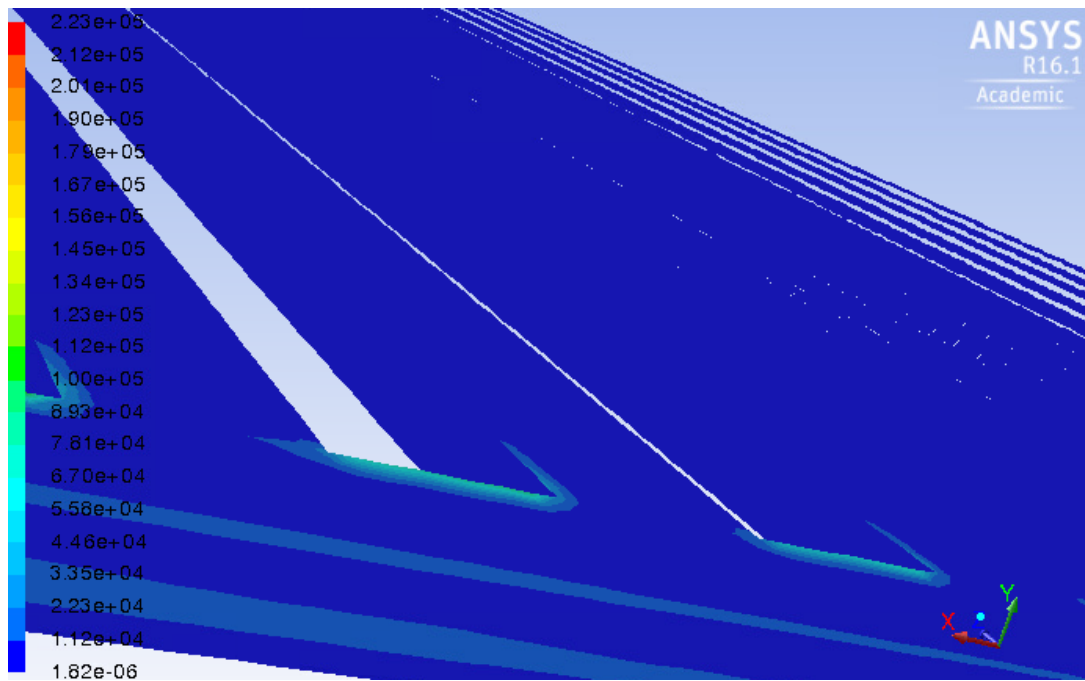


Figure 36: Contours of the volume integral of the temperature component of the entropy near at the inlet region with an inlet velocity of 0.05 m/s

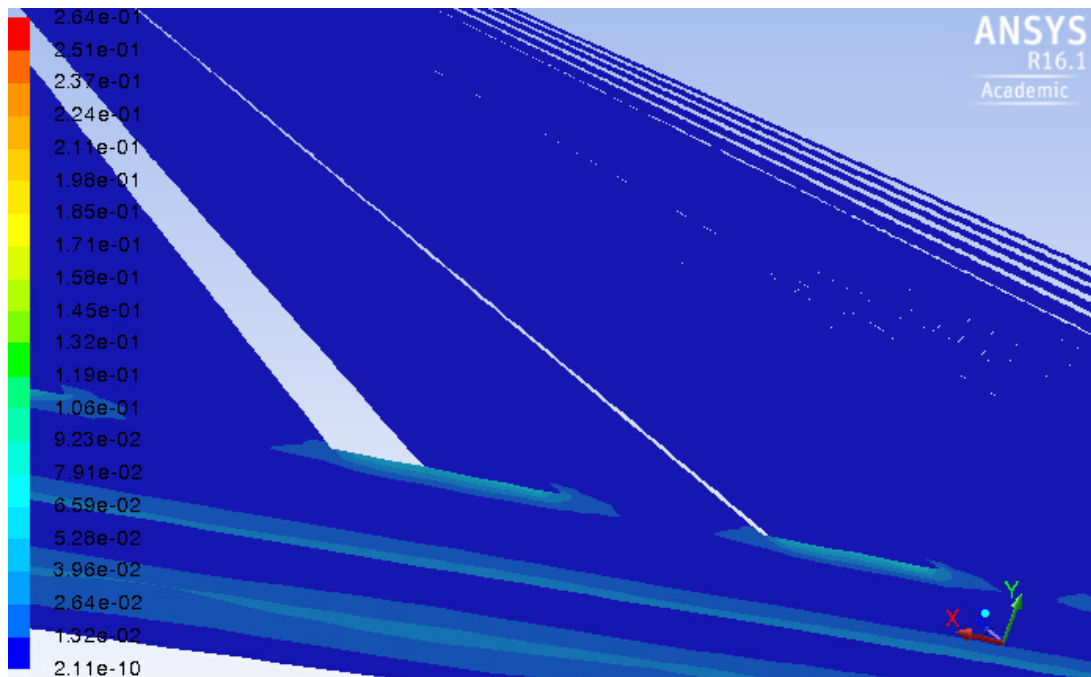


Figure 37: Contours of the volume integral of the heat dissipation of entropy at the inlet region with an inlet velocity of 0.05 m/s

Appendix E-2: SFF Results

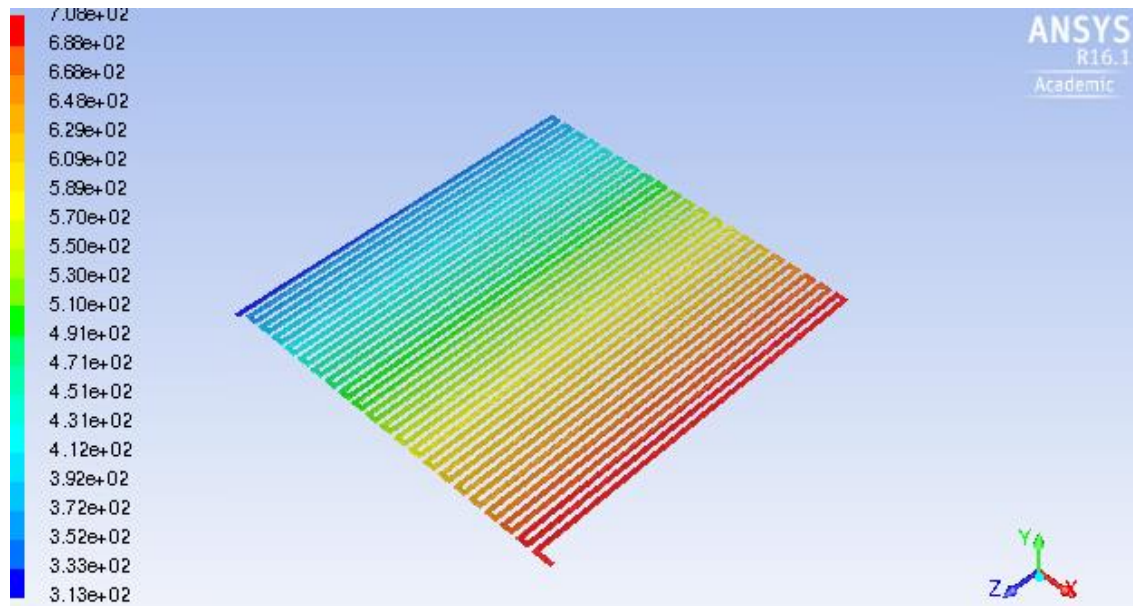


Figure 38: Contours of the temperature distribution in fluid with an inlet velocity of 0.05 m/s

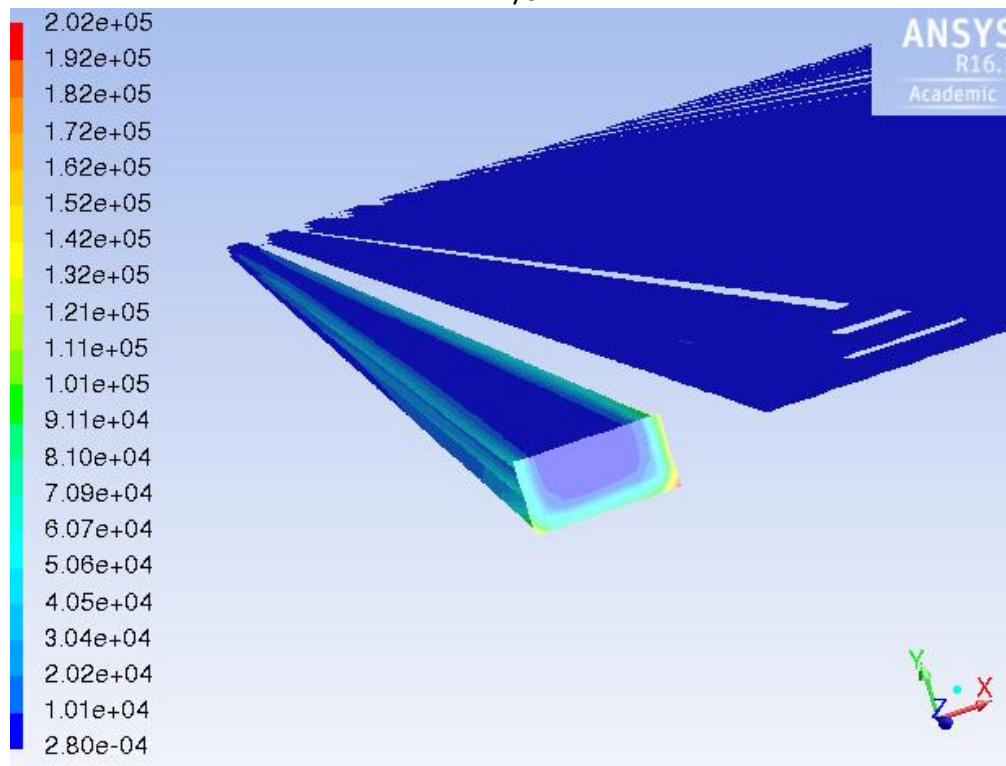


Figure 39: Contours of the volume integral of entropy at the inlet region with an inlet velocity of 0.05 m/s

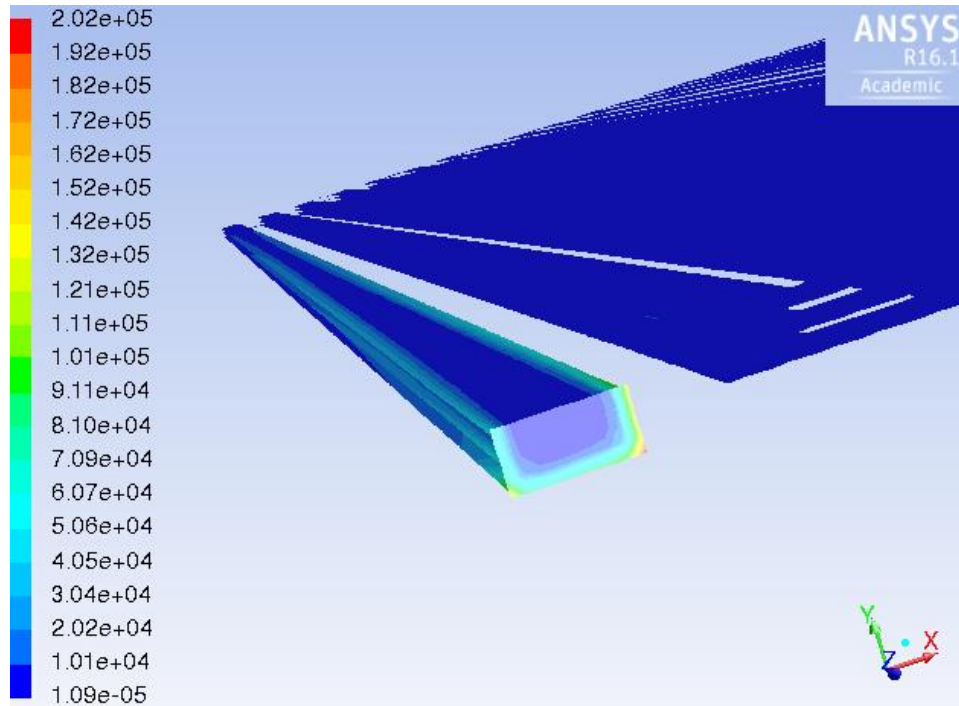


Figure 40 Contours of the volume integral of the temperature component of the entropy near at the inlet region with an inlet velocity of 0.05 m/s

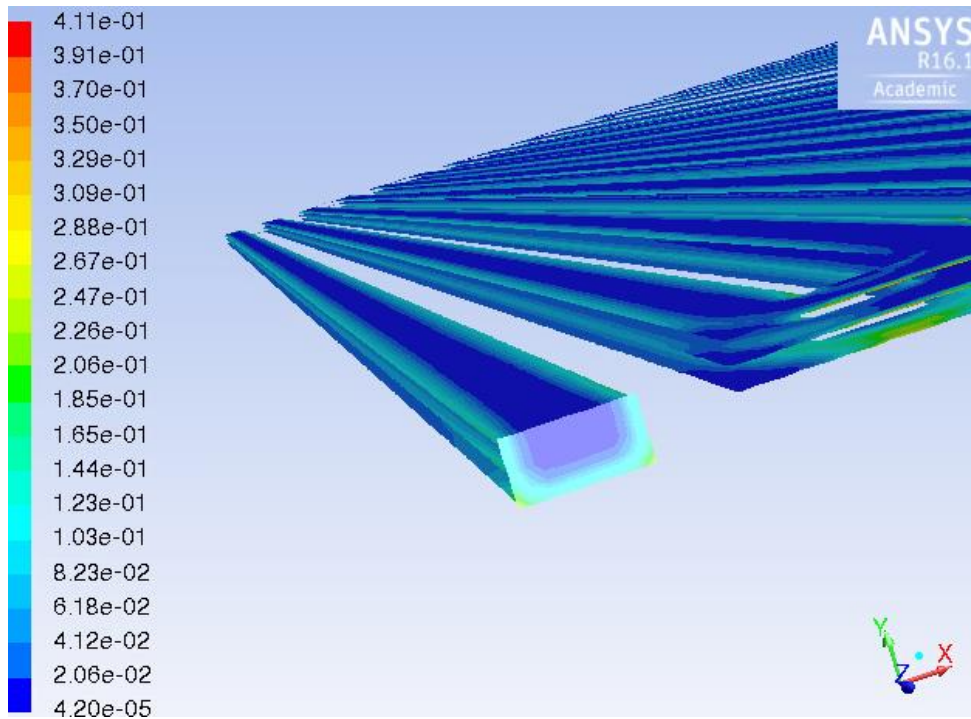


Figure 41 Contours of the volume integral of the heat dissipation of entropy at the inlet region with an inlet velocity of 0.05 m/s

Appendix E-3: PFF Results

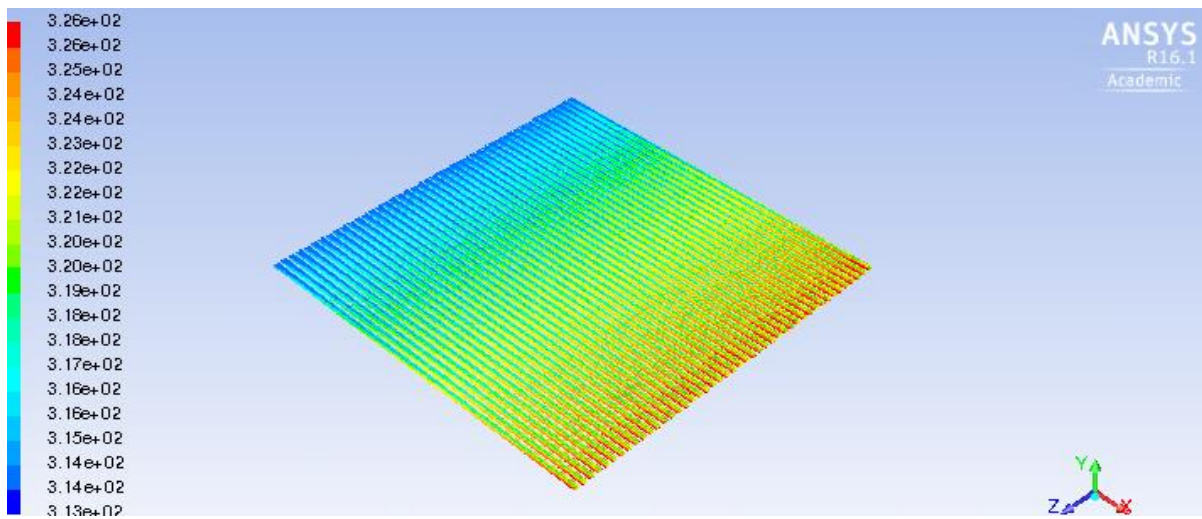


Figure 42: Contours of the temperature distribution in fluid at an inlet velocity of 0.05 m/s

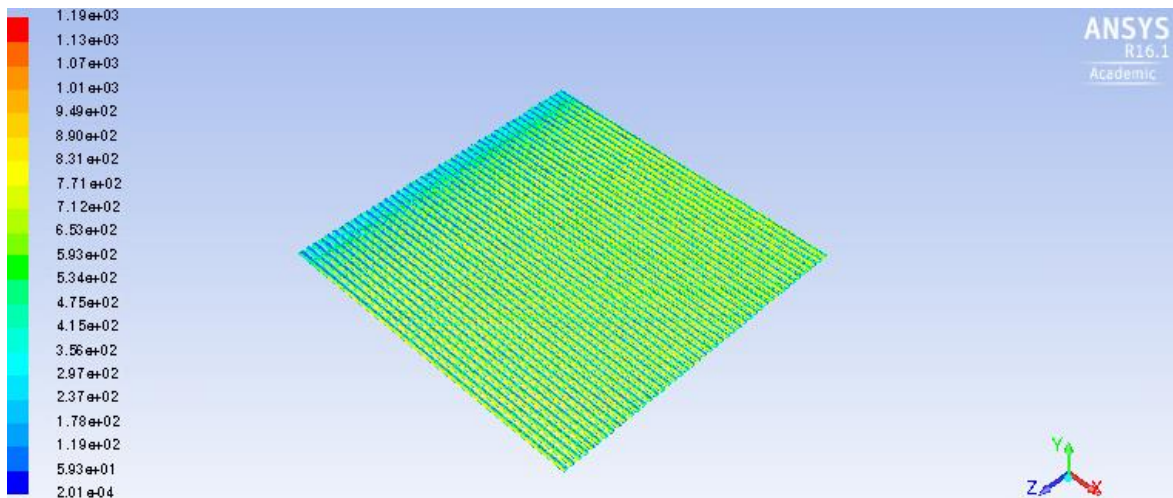


Figure 43: Contours of total entropy distribution in fluid at an inlet velocity of 0.05m/s